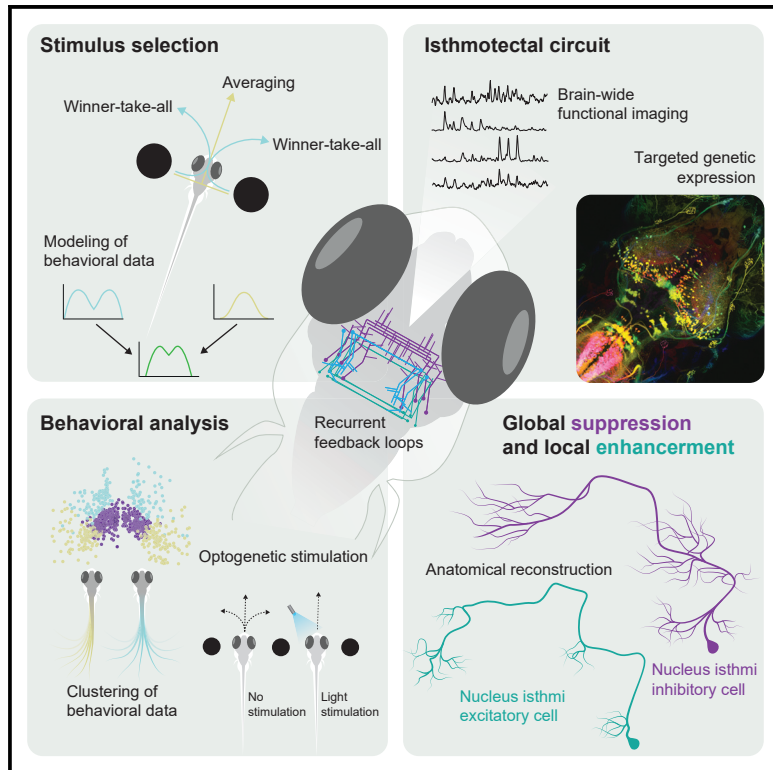


Neural circuitry for stimulus selection in the zebrafish visual system

Graphical Abstract



Authors

António M. Fernandes,
Duncan S. Mearns,
Joseph C. Donovan, ...,
Koichi Kawakami, Marco dal Maschio,
Herwig Baier

Correspondence

hbaier@neuro.mpg.de

In Brief

Fernandes et al. investigate how zebrafish larvae respond selectively to one of two stimuli competing for the animal's attention. Two strategies for stimulus selection are used: winner-take-all or averaging. The corresponding neuronal computations are implemented in an intricate system of feedback loops between tectum and nucleus isthmi.

Highlights

- Zebrafish respond to competing stimuli using winner-take-all and averaging strategies
- Retinotectal and isthmotectal circuits enable context-dependent stimulus selection
- Perturbing nucleus isthmi function disrupts behavioral action selection
- Isthmotectal circuit layout is consistent with local enhancement and global suppression



Article

Neural circuitry for stimulus selection in the zebrafish visual system

António M. Fernandes,¹ Duncan S. Mearns,^{1,2} Joseph C. Donovan,¹ Johannes Larsch,¹ Thomas O. Helmbrecht,^{1,2} Yvonne Kölsch,^{1,2} Eva Laurell,¹ Koichi Kawakami,³ Marco dal Maschio,^{1,4} and Herwig Baier^{1,5,*}

¹Department Genes-Circuits-Behavior, Max Planck Institute of Neurobiology, 82152 Martinsried, Germany

²Graduate School of Systemic Neurosciences, LMU BioCenter, Grosshaderner Strasse 2, 82152 Martinsried, Germany

³Laboratory of Molecular and Developmental Biology, National Institute of Genetics, Department of Genetics, SOKENDAI (The Graduate University for Advanced Studies), Mishima, Shizuoka 411-8540, Japan

⁴Present address: Department of Biomedical Sciences, Padua Neuroscience Center, University of Padua, via Ugo Bassi 58B, 35131 Padova, Italy

⁵Lead contact

*Correspondence: hbaier@neuro.mpg.de

<https://doi.org/10.1016/j.neuron.2020.12.002>

SUMMARY

When navigating the environment, animals need to prioritize responses to the most relevant stimuli. Although a theoretical framework for selective visual attention exists, its circuit implementation has remained obscure. Here we investigated how larval zebrafish select between simultaneously presented visual stimuli. We found that a mix of winner-take-all (WTA) and averaging strategies best simulates behavioral responses. We identified two circuits whose activity patterns predict the relative saliences of competing visual objects. Stimuli presented to only one eye are selected by WTA computation in the inner retina. Binocularly presented stimuli, on the other hand, are processed by reciprocal, bilateral connections between the nucleus isthmi (NI) and the tectum. This interhemispheric computation leads to WTA or averaging responses. Optogenetic stimulation and laser ablation of NI neurons disrupt stimulus selection and behavioral action selection. Thus, depending on the relative locations of competing stimuli, a combination of retinotectal and isthmotectal circuits enables selective visual attention.

INTRODUCTION

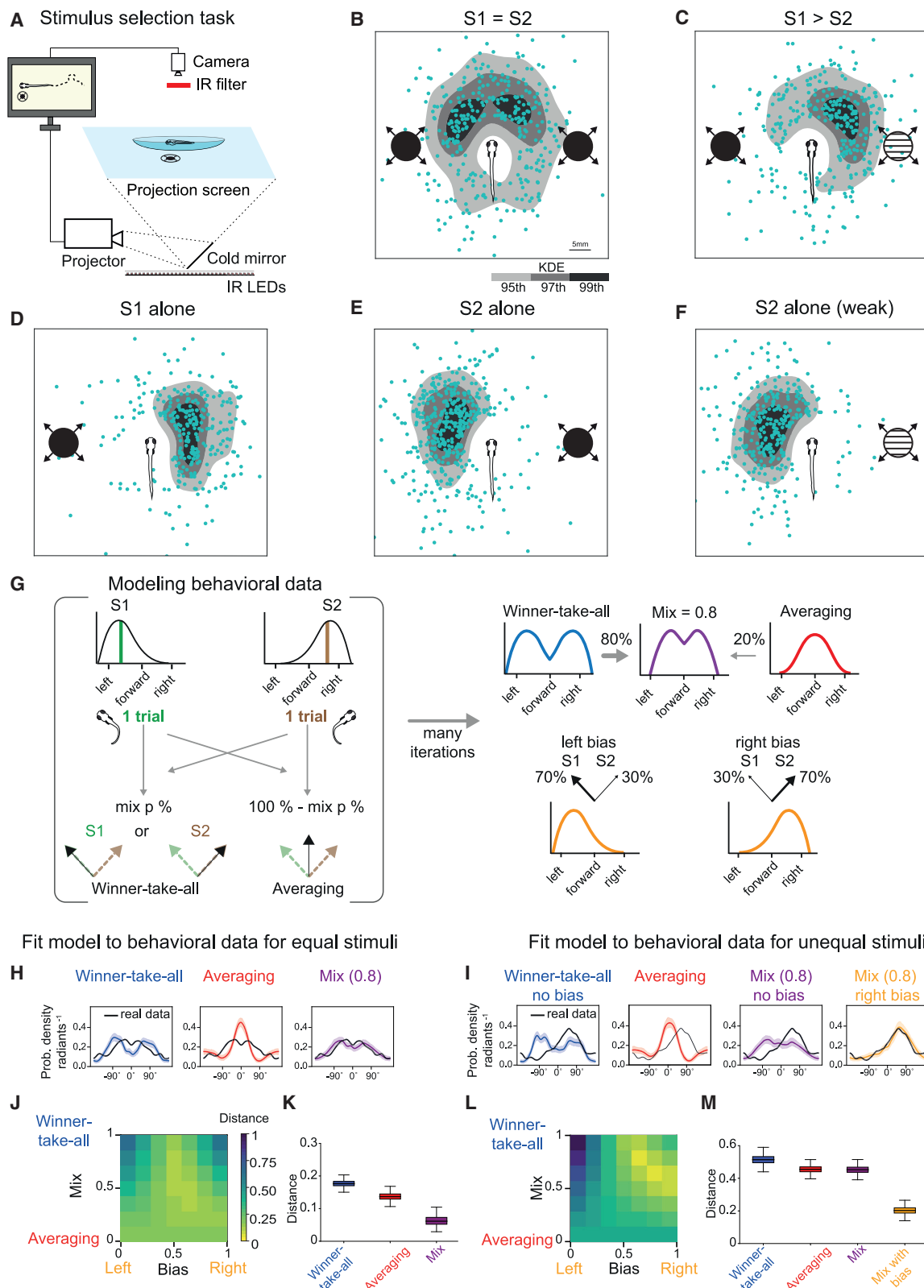
When confronted with a crowded visual scene, animals often choose a single object for a behavioral response from multiple competing stimuli. Examples of such stimulus selection include escaping from the most imminent among several approaching threats or focusing on one individual prey item within a herd or shoal. Elementary forms of spatial attention exist in many species, including flies (Sareen et al., 2011), fish (Ben-Tov et al., 2015), and mice (Wang and Krauzlis, 2018). Winner-take-all (WTA) computations, in which an animal responds to a single target while disregarding others, are considered to be crucial during bottom-up, stimulus-driven attention (Itti and Koch, 2000). In addition to WTA mechanisms, evidence suggests that presentation of multiple visual targets in primates can also lead to gaze shifts toward their mean locations (Lisberger and Ferrera, 1997; Nummela and Krauzlis, 2011; Ottes et al., 1984). In contrast to the WTA strategy, this “averaging” mode suggests the existence of a neurocognitive process that integrates across competing sensory stimuli rather than selecting a single stimulus for a response.

It has been postulated that, during decision-making, multiple potential actions are represented in the brain and that these par-

allel representations compete against each other (e.g., Cisek, 2007). According to this view, the relative importance of targets across the visual field is represented in the brain through circuit mechanisms that focally enhance the response to the salient stimulus and globally suppress neuronal activity elsewhere (Ewert, 1997; Koch and Ullman, 1985; Lee et al., 1999). Such a “saliency map” appears to be implemented in the tectum/superior colliculus of vertebrates as distantly related as lampreys, goldfish, birds, and primates (e.g., Gruberg et al., 2006; Kardamakis et al., 2015; Knudsen, 2018; Krauzlis et al., 2018; Schellart et al., 1979; Zhaoping, 2016). Studies in the barn owl tectum suggest that stimulus competition could be supported by a neuronal circuit with reciprocal loops between the tectum and the nucleus isthmi (NI), a satellite nucleus, which is homologous to the parabigeminal nucleus of mammals and is located in the tegmentum (Knudsen, 2018). Evidence for this model has come mainly from single-cell electrophysiology and classical tract-tracing studies.

Here we investigated the behavioral decisions of zebrafish larvae when they are faced with two competing threatening stimuli. We found that escape direction is determined by WTA and averaging strategies, which are implemented to varying degrees by individual fish. Brain-wide two-photon functional imaging, targeted cell ablations, and optogenetic stimulation of identified





(legend on next page)

neuronal populations revealed two circuits impinging on the tectum that contribute to stimulus selection in a location-dependent manner. When both stimuli are presented to the same eye, the saliency computation is already detectable in the activity of retinal ganglion cell terminals in the tectum. When the two stimuli are presented to different eyes, an isthmotectal pathway, forming recurrent feedback loops between the NI and the tectum, weighs the relative stimulus strengths and is required for target selection across hemispheres. These results pinpoint neural circuitries for intra- and interhemispheric stimulus competition in a vertebrate visual system.

RESULTS

A WTA strategy predominates behavioral responses to competing stimuli

To identify the strategies adopted in response to competing stimuli, we established a stimulus selection paradigm for zebrafish larvae. We tracked individual larvae swimming freely in an arena using computer vision. Based on its location, visual stimuli were projected from below at defined positions relative to the animal's orientation (Figure 1A). The stimulus consisted of one or two looming disks of defined expansion rate and contrast. Dark expanding stimuli, mimicking an approaching predator or an object on a collision course, are strongly aversive for zebrafish and lead to a vigorous escape movement (Bhattacharyya et al., 2017; Dunn et al., 2016; Temizer et al., 2015). Single looming disks presented to one side of the fish were highly effective in driving an escape response to the opposite side (Figures 1D–1F and S1). Depending on the location and the strength of the stimulus, larvae adjusted the direction and magnitude of their response. Increasing the expansion rate or contrast of the stimulus resulted in a higher probability and greater vigor of escape responses (Figures S1A–S1E, S1I, and S1J). These observations confirm earlier studies that larval zebrafish adapt their behavior to the strength of a looming stimulus (Bhattacharyya et al., 2017).

Next we wanted to find out how larvae respond to two stimuli presented simultaneously at different locations. We dis-

played two looming stimuli to the same eye in non-overlapping parts of the visual field (Figure S2A), first alone and then in combination. A single looming disk positioned in the anterior visual field triggered a sideways escape ($82.5^\circ \pm 75$, mean \pm standard deviation [SD]) with respect to the heading direction; Figures S2B, S2E, and S2L, whereas a posteriorly located disk triggered a forward escape ($47^\circ \pm 41$ SD; Figures S2C, S2H, and S2L). For two identical stimuli, we expected either a stochastic choice or an escape trajectory corresponding to the average of the two locations. If the two stimuli differ, the more salient stimulus should dominate the response. In this case, the escape direction may still be a weighted average of the stimulus strengths. Both stimuli presented together yielded a distribution of escape angles that included the responses to single stimuli (Figures S2D and S2G). As expected by a WTA strategy, the faster of the two stimuli dominated the escape direction so that the mean response angle was similar to that triggered by a single stimulus presented at the same position (Figures S2F, S2I, and S2J–S2L).

For two looming objects presented to opposite sides of the fish, we observed a bimodal distribution of escape trajectories. When the two disks expanded at identical rates, this distribution was largely symmetrical around the heading direction. Thus, larvae escaped in a direction away from one, apparently randomly chosen disk (Figures 1B and S1G). Modulating the expansion rate of one stimulus biased escapes away from the faster stimulus (Figures 1C and S1H). These observations indicate that larvae adapt the direction and magnitude of their behavioral response to the location and strength of the more salient stimulus.

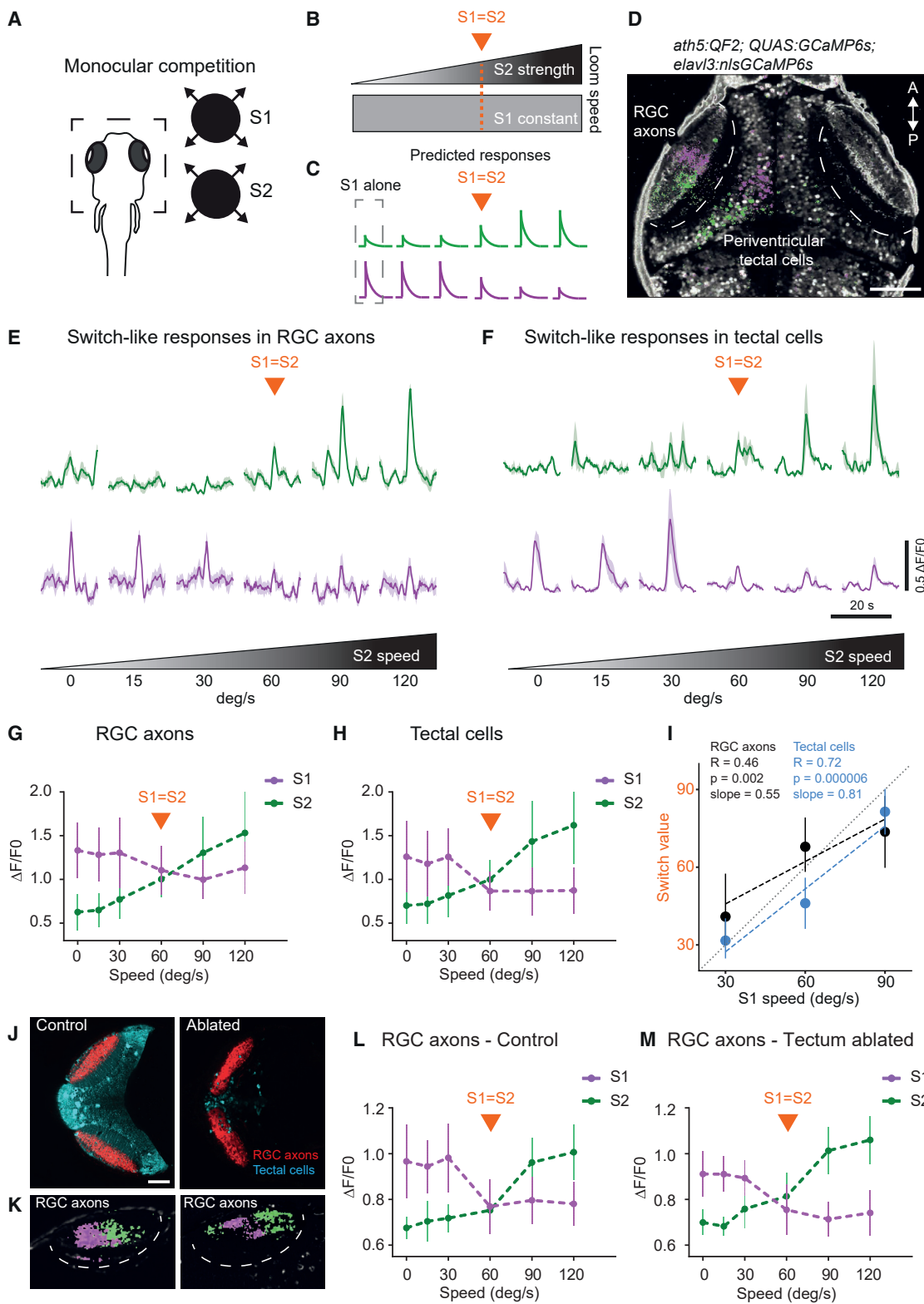
Modeling reveals that fish larvae use a mixture of WTA and averaging strategies

Although WTA-mediated escapes comprise many responses (approximately 80%), a notable fraction of responses (approximately 20%) had a heading between the two stimuli, a behavior best explained by an averaging strategy. To estimate the relative contributions of each strategy, we fit the data with a model that

Figure 1. Zebrafish respond to competing stimuli according to their relative saliences

- (A) Schematic of the stimulus selection task. The animal is tracked while updating, in real time, the positions of the looming disks projected from below.
- (B) Presentation of equal stimuli ($S_1 = S_2, 90^\circ/\text{s}$). Blue dots are XY positions of fish after escape. In grayscale are kernel density estimation (KDE) isocontours of the same data. Fish schematics are enlarged for clarity.
- (C) Competition between unequal stimuli ($S_1 > S_2, 90^\circ/\text{s}$ versus $60^\circ/\text{s}$).
- (D) Response to a single looming stimulus (S_1 alone, $90^\circ/\text{s}$) presented on the left side of the fish.
- (E) Same stimulus presented to the right side of the fish.
- (F) Weaker stimulus ($S_2, 60^\circ/\text{s}$) presented on the right side.
- (G) Implementation of a WTA, averaging, and mixed strategy models to explain observed behavioral data. Mix adjusts the amount of WTA relative to averaging. Bias adjusts the probability of response for S_1 versus S_2 to accommodate unequal stimuli. A bias parameter equal to 0.5 corresponds to no bias left or right (50% chance of a fish selecting either of two looming stimuli).
- (H) Modeling of behavior for equal stimulus competition. Shaded areas are 95% confidence intervals (CIs).
- (I) Similar to (H) but for unequal stimuli.
- (J) Behavior reconstruction goodness of fit. Heatmap showing the normalized energy distance between model and real data (related to H) depending on the model parameters (bias and mix).
- (K) Boxplot quantification of model energy distance to the real data using resampling statistics. Permutation test p values that the mix model outperforms the simpler models are as follows: WTA, 0.0001; averaging, 0.008. For details, see STAR methods.
- (L) Similar to (J) but for unequal stimuli.
- (M) Similar to (K) but for unequal stimuli. Permutation test p values that the mix bias model outperforms the simpler models are $p < 0.001$ (WTA), $p < 0.001$ (averaging), and $p < 0.001$ (mix model).

$n = 117$ fish.



(legend on next page)

mixed predictions from both behavioral strategies (Figure 1G). Models where WTA outweighed averaging provided a better fit for the behavioral data when stimuli had equal strengths (Figures 1H, 1J, 1K, S1K, and S1L). For unequal stimuli, we found that the fish responded more often to the faster looming disk. This asymmetry could be modeled by adding a bias term, where 0.5 is balanced and other values reflect asymmetry, to the WTA component of the model while keeping the same relative mixture of WTA and averaging (Figures 1I, 1L, 1M, S1M, and S1N).

Observing the responses of single animals revealed that individual larvae could switch between WTA and averaging strategies (Figure S1P). We conclude that both strategies are implemented in the same brain and are called up in a context-dependent manner. The exact conditions, experience, or internal states that bias the underlying circuits to choose the WTA over the averaging mode and vice versa are not known.

Tectal neurons exhibit WTA dynamics in response to competing stimuli

We next investigated the neural correlates of stimulus selection using brain-wide calcium imaging. First we determined which regions of the brain respond reliably to looming stimuli. Monocular presentation activated retinal ganglion cell (RGC) axons, the tectum, the pretectum, and a thalamic area near retinal arborization field 4 (AF4) (Heap et al., 2018; Temizer et al., 2015; Figure S3A). In addition, our recordings revealed a responsive area located at the midbrain-hindbrain boundary, a location that coincides with the expected position of the NI (Gruberg et al., 2006; Northmore, 1991; Northmore and Gallagher, 2003).

For implementation of a WTA strategy, at least two neuronal response types need to be present: (1) neurons whose activity scales with the strength of one stimulus and (2) neurons whose activity is suppressed by a more salient competitor (Knudsen, 2018). To search for these response signatures, we kept the expansion rate of one looming stimulus constant (S1) while systematically varying the expansion rate of a

competitor (S2) (Figures 2A–2C). We used transgenic fish expressing cytosolic genetically encoded calcium indicator GCaMP6s in RGCs and nucleus-localized GCaMP6s in all neurons. This approach enabled simultaneous recording and unambiguous separation of RGC axon activity in the tectal neuropil layers from tectal cell activity in the cell body layer. As expected, the activity elicited by monocular presentation of S1 and S2 was organized retinotopically, leading to non-overlapping response foci in the anterior or posterior tectal cells and neuropil, respectively (Figure 2D).

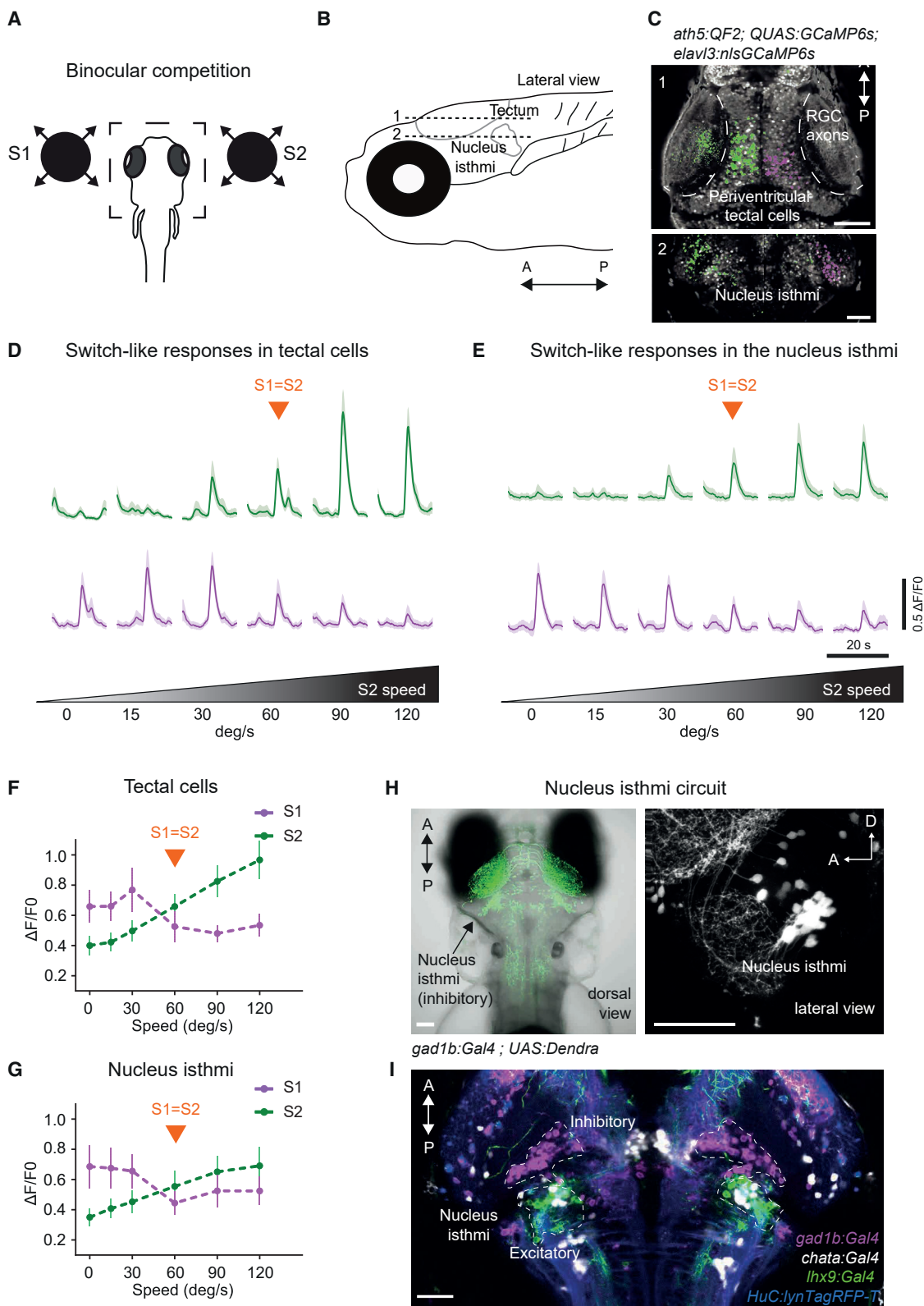
Presenting two competing stimuli to the same eye resulted in a variety of responses in the tectum. Some responses scaled with increasing S2 expansion rate (Figures 2F and 2H, green traces). On the other hand, a subset of S1-responsive tectal cells was suppressed when S2 was stronger or identical to S1 and enhanced when S2 was weaker than S1 (Figures 2F and 2H, magenta traces). This switch-like tuning is consistent with stimulus competition by reciprocal inhibition (Mysore and Knudsen, 2012). Thus, functional imaging revealed the presence of neurons in the tectum whose activity scales with the strength of one stimulus and neurons whose activity is suppressed by a salient competitor, consistent with the predictions of a WTA model.

Monocular WTA dynamics are implemented in the inner retina

For two looming stimuli visible to the same eye, we observed switch-like responses not only in tectal cells but already at the level of the RGC axonal projections to the tectum (Figures 2E and 2G). The switch transition for the population response was flexible and shifted systematically with the strength of S1 (Figures 2I and S3B–S3G). We noticed that tectal cells better predicted the switch value compared with RGCs (difference between correlations: Fisher's z-transformation $p = 0.039$; Figure 2I). We conclude that monocular stimulus competition manifests in reduced activity of RGC axons and is sharpened further in the tectum.

Figure 2. Activity of RGCs and tectal neurons exhibit switch-like responses during monocular competition

- (A) Schematic of the calcium imaging experiment. Right: monocular competition task. S1, stimulus 1; S2, stimulus 2.
- (B) Schematic of the competition protocol. The orange line represents the condition with presentation of equal stimuli (switch value).
- (C) Predicted responses following a strategy resembling WTA.
- (D) Pixel-wise regression analysis of the temporal series during a single imaging trial. The corresponding t -statistic for each pixel is calculated (only pixels that passed a threshold using the 90th percentile are shown). Map shows associated S1-responsive pixels suppressed by a stronger S2 (magenta) and pixels with enhanced responses as a function of S2 strength (green). Scale bar, 50 μ m.
- (E) Characteristic activity profiles for RGCs. Top traces, average of 10 RGC axon regions of interest (ROIs) enhanced by S2 (in green). Lower traces, average of 10 RGC axon ROIs suppressed by a stronger S2 (in magenta). The orange arrow represents the condition with presentation of equal stimuli (switch value).
- (F) Similar to (E) but for tectal cells.
- (G) Summary plot across all conditions for RGC axon pixels. Switch-like responses, showing RGC pixels suppressed by S2, are shown in magenta. RGC pixels enhanced by S2 are shown in green. The S1 expansion rate is 60°/s.
- (H) Similar to (G) but for tectal pixels.
- (I) Switch value increases with S1 strength for RGC axons and tectal cells. The R value is the correlation coefficient. The p value relates to testing whether the slope is zero. n = 5 fish.
- (J) Chemogenetic ablation of tectal cells does not affect suppression observed in RGC axons. The genotype used were *ath5:QF2*, QUAS:GCaMP6s (red), SAGFF(LF)81C, and UAS:NTR-mCherry (cyan). Left: control fish. Right: ablated fish. Scale bar: 100 μ m.
- (K) Pixel-wise regression analysis of the temporal series during a single imaging trial. The corresponding t -statistic for each pixel is calculated as in (D). The map shows associated S1-responsive pixels suppressed by a stronger S2 (magenta) and pixels that enhance their responses as a function of S2 strength (green). Left panel: control fish. Right panel: ablated fish.
- (L) Summary plot across all conditions for RGC axon pixels. Switch-like responses, showing RGC pixels suppressed by S2, are shown in magenta. RGC pixels enhanced by S2 are shown in green. The S1 expansion rate is 60°/s. Control fish. n = 4 fish.
- (M) Similar to (L) but for ablated fish. n = 5 fish. Error bars indicate SD.



(legend on next page)

To test whether RGC modulation was due to feedback from the tectum (Henley et al., 1986), we imaged GCaMP6s-labeled retinal axon terminals following chemogenetic ablation of nitroreductase-expressing tectal neurons (Figures 2J, 2K, and S4J). Treatment with the cell-death-inducing pro-toxin metronidazole led to severe impairments in behavioral responses to looming and prey stimuli (Figures S4D–S4G). Switch-like responses of RGCs, however, remained intact (Figure 2L and 2M; $p = 0.1797$, two-way Mann-Whitney test). These results indicate that stimulus competition already shapes neuronal responses in the inner retina and does not require retrograde modulation by tectal cells.

Retinotectal WTA is a general mechanism for stimulus selection independent of valence

Synthetic prey-like objects have been shown previously to evoke hunting behavior in zebrafish larvae (Bianco et al., 2011; Semmelhack et al., 2014). We tested whether the WTA dynamics observed in response to two looming disks extend to the response to two small, motile dots that simulate prey. As with looming stimuli, RGC axons and tectal responses showed suppression and enhancement driven by competing prey-like stimuli (Figures S4A–S4C). Such a mechanism might serve efficient target selection during hunting against a background of distractors. This finding indicates that stimulus competition in the retinotectal system is a global mechanism, not restricted to looming stimuli, and guides diverse natural behaviors.

Tectal and isthmic neurons show WTA responses to competing binocular stimuli

Based on previous work in birds, the NI is a prime candidate for shaping tectal responses to binocular competing stimuli (Figure 3A). Indeed, in response to concurrent stimuli presented to each eye, we observed WTA dynamics in both tectal hemispheres and the NI (Figures 3B and 3C). The activity patterns of left and right hemispheres were unbalanced; when one tectal hemisphere had high activity, the other hemisphere had low activity, mirroring the relative strengths of the stimuli (Figures 3C–3E). Similar to monocular competition, we found S1-responsive neurons that were inhibited by a stronger S2 and stimulus-selective neurons that enhanced their response as a function of either S1 or S2 intensity (Figures 3D–3G). This switch-like suppression

and enhancement matched our predicted WTA signature and thus identifies a neural correlate of interhemispheric spatial attention.

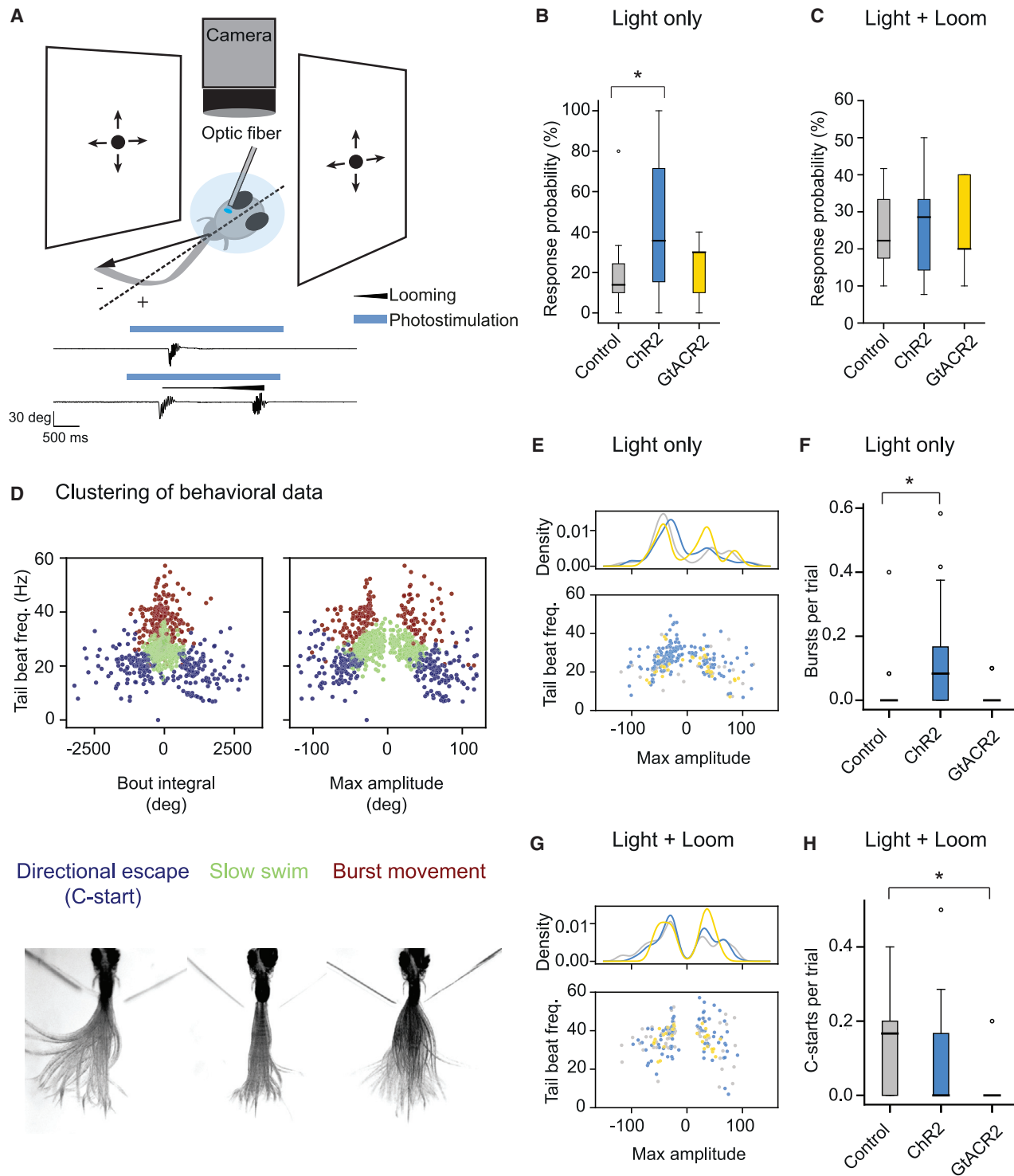
To characterize the cellular composition of the NI, we used transmitter-specific Gal4 lines, RNA *in situ* hybridization, and immunohistochemistry to label glutamatergic (*vglut2a* and *lhx9*), cholinergic (choline acetyltransferase, ChAT), and GABAergic neurons (Figures 3H, 3I, and S5). Co-registration of these lines and markers within a standard brain (Kunst et al., 2019) revealed that the glutamatergic and GABAergic populations form two spatially segregated clusters close to the midbrain-hindbrain boundary (Figure 3I). A small subset of *lhx9*-positive, glutamatergic neurons co-express ChAT (Figures S5F). NI cells express known marker genes for the isthmic region, e.g., Reelin (Figure S5; Volkmann et al., 2010) and project mainly to the tectum (Figure 3H, right panel). The vast majority of GABAergic and glutamatergic NI neurons labeled in the lines used here respond to looming stimuli; only a small fraction to prey-like or dimming stimuli (Figures S6A and S6D). Functional imaging during binocular competition revealed that glutamatergic and GABAergic NI populations displayed switch-like activity (Figures S6B and S6E). However, only glutamatergic neuronal activity scaled significantly with the strength of the distractor S2 (Figures S6G–S6K). These data suggest that NI neurons show responses compatible with their function in generating a saliency map.

Inhibition of the NI reduces the number of WTA behavioral responses

Next we wanted to identify the functional role of the NI in generating behavioral responses to competing looming stimuli. To this end, we developed a restrained preparation that allowed us to selectively activate or inhibit the NI while presenting looming stimuli to both eyes (Figure 4A). In the absence of visual stimulation, we found that optogenetic activation of *lhx9*-positive NI neurons using ChR2 was more than twice as likely to induce swimming behavior compared with ChR2– controls (ChR2+, response probability = 0.44 ± 0.34 , $n = 21$ fish; control, response probability = 0.19 ± 0.17 , $n = 18$; mean \pm SD; $p = 0.0217$; Figure 4B). Inhibition of the same NI population using GtACR2 neither increased nor suppressed swimming responses to the light (response probability = 0.21 ± 0.14 , $n = 9$, $p = 0.189$

Figure 3. WTA dynamics in tectal and isthmic neurons in response to competing binocular stimuli

- (A) Binocular competition task.
- (B) Anatomical location of the tectum (plane 1) and the NI (plane 2).
- (C) Pixel-wise regression analysis during a single imaging trial. The *t*-statistic for each pixel is calculated as in Figure 2D. Map 1 shows associated S1-responsive tectal pixels suppressed by a stronger S2 stimulus (in magenta). Pixels that enhance their response as a function of S2 intensity are shown in green. Map 2: similar to Map 1 but for the NI. Scale bars, 50 μ m.
- (D) Characteristic activity profiles for tectal cells. Top traces, average of 10 tectal ROIs enhanced by S2 (green). Lower traces, average of 10 tectal ROIs suppressed by a stronger S2 stimulus (magenta).
- (E) Similar to (D) but for NI.
- (F) Summary plot across all conditions for tectal pixels. Switch-like responses, showing pixels suppressed by S2, are shown in magenta. Pixels enhanced by S2 are shown in green. $n = 5$ fish.
- (G) Similar to (F) but for NI. $n = 4$ fish. Error bars indicate SD.
- (H) Dorsal image of a double-transgenic *gad1b:Gal4VP16^{mpn155}*; *UAS:Dendra-kras^{s1998t}* fish, labeling GABAergic neurons in green. The arrow indicates the location of GABAergic NI neurons. Right panel, lateral view of *gad1b:Gal4VP16^{mpn155}*; *UAS:nfsb-mCherry^{c264}* fish, labeling GABAergic neurons in white.
- (I) Alignment of several transgenic lines: *gad1b:Gal4VP16^{mpn155}* labeling GABAergic NI neurons (magenta), *lhx9:Gal4VP16^{mpn203}* labeling *lhx9*-positive NI neurons (green), and *chata:Gal4VP16^{mpn202}* labeling cholinergic NI neurons (white). *elavl3:lyn-tagRFP^{mpn404}* is used as a reference channel (blue). Scale bars, 50 μ m.

**Figure 4. Optogenetic manipulation of the NI during presentation of competing binocular looming stimuli**

(A) Schematic of the optogenetics setup. A fish is embedded in agarose with the tail free. The tail is recorded with a camera. Equal looming stimuli are presented to both eyes simultaneously. NI is stimulated unilaterally with an optical fiber. Negative angles represent tail deflections toward the stimulated side, and positive angles represent tail deflections away from the stimulated side. Bottom: example trials from a fish expressing ChR2 in the NI. Shown are photostimulation only (top) and photostimulation with looms (bottom). Black traces show tail angle over time. The blue bar represents time of optogenetic stimulation. The black line above the tail trace triangle represents the duration of loom.

(legend continued on next page)

compared with controls). Notably, we found that neither excitation nor inhibition of *lhx9*-positive cells in the NI affected the probability of responding to looming stimuli (response probabilities = 0.24 ± 0.10 , controls; 0.26 ± 0.12 , ChR2+; 0.27 ± 0.11 , GtACR2+) (Figure 4C). These results demonstrate that activity within the excitatory cells of the NI is sufficient to drive behavioral responses.

We next sought to identify what kinds of swim bouts larvae performed in response to optogenetic and visual stimulation. We identified all bouts in the dataset, including light-evoked, looming-evoked, and spontaneous bouts that occurred outside the stimulation period ($n = 881$ bouts total) and characterized each bout based on three kinematic parameters (bout integral, maximum tail amplitude, and tail beat frequency). We then performed hierarchical clustering in this kinematic space and identified three primary bout types (Figure 4D; STAR Methods). C-starts were characterized by a large maximum tail amplitude and large bout integral (Burgess and Granato, 2007; Figure 4D, blue cluster). Burst swims exhibited a high tail beat frequency and were symmetric across the midline (Budick and O'Malley, 2000; Figure 4D, red cluster). Slow swims exhibited relatively small values across all three parameters (Figure 4D, green cluster). These slow swims appeared to encompass routine turns and slow 1 and slow 2 swims described previously (Marques et al., 2018). We found that activation of the NI in the absence of visual stimuli predominantly drove slow swims that were biased ipsilaterally to the stimulation site (Figure 4E). Interestingly, we were also able to elicit a small but significant number of burst swims in multiple animals (ChR2+, number of swims = 0.13 ± 0.16 per trial; control, number of swims = 0.03 ± 0.09 ; mean \pm SD; $p = 0.0026$; Figure 4F). These results suggest that the NI is sufficient to release fast forward swimming as well as slow orientation behaviors.

Finally, we investigated the bouts fish performed in response to competing looming stimuli. In control animals not expressing any optogenetic effector, we found evidence of WTA (C-starts) and averaging (burst swims) behavioral dynamics, consistent with our observations from free-swimming larvae (Figure 1). In this restrained preparation, we found that an averaging response was more likely than WTA (0.44 ± 0.34 burst swims per loom, 0.12 ± 0.12 C-start per loom, mean \pm SD). Surprisingly, we found that, even though NI stimulation in isolation was sufficient to drive burst swims, we were unable to drive additional burst swims in response to competing looms upon ChR2 stimulation (0.50 ± 0.33 per loom, $p = 0.21$ compared with controls). This

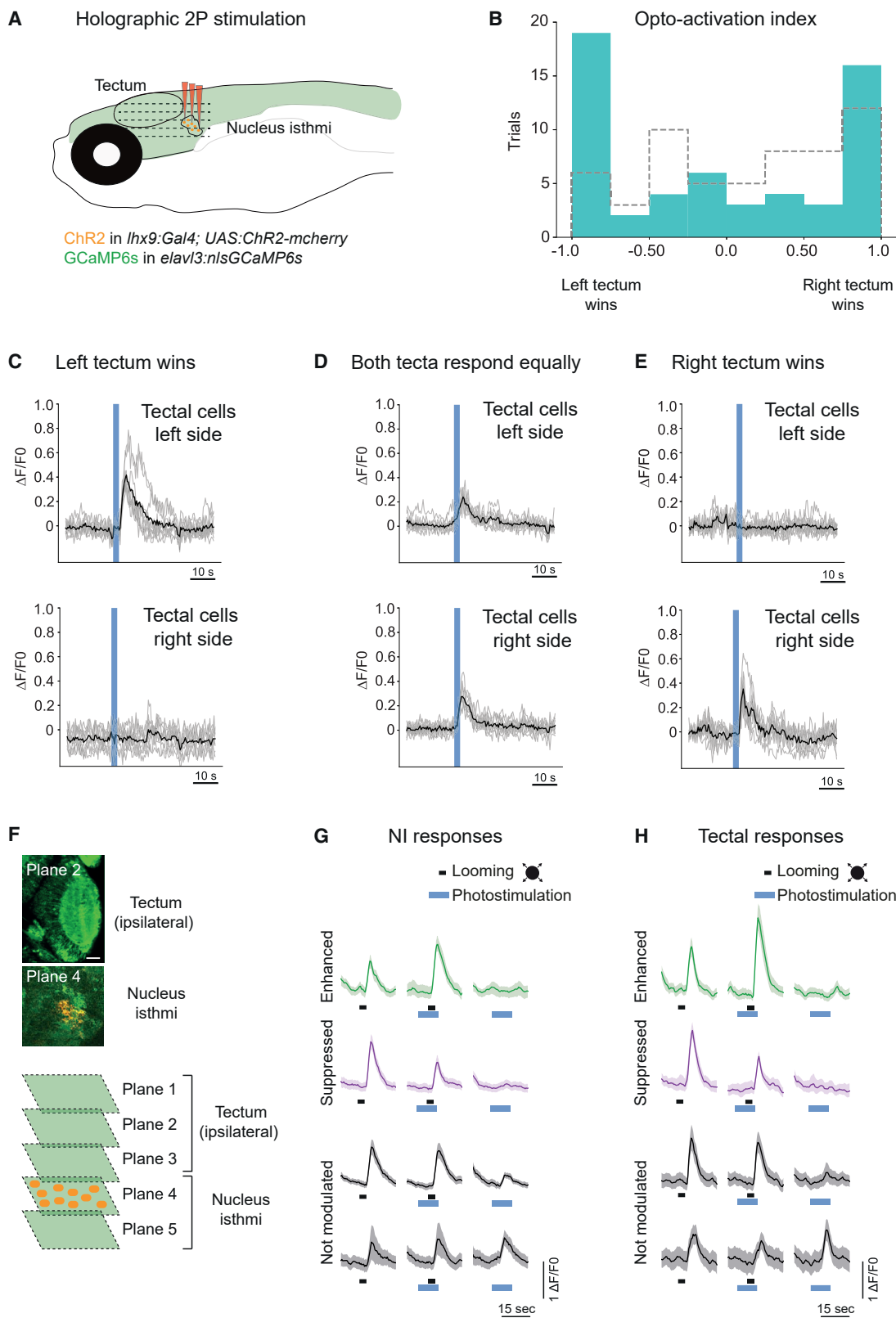
may be a result of a ceiling effect, with averaging strategies already dominating in this behavioral paradigm, or due to optogenetic stimulation being insufficient to override innate responses to looming stimuli (Klapoetke et al., 2017). Inhibition of *lhx9*-positive NI cells during the presentation of looming stimuli, however, decreased the number of C-starts elicited by around 80% (0.02 ± 0.06 C-starts per trial, $p = 0.020$ compared with controls) (Figure 4H). Neither excitation nor inhibition of the NI biased the direction of elicited C-starts (Figure 4G), suggesting that the direction of an escape is not determined by the activity in one nucleus in isolation. These results suggest that the NI plays an instructive role in generation of behavior in response to competing looming stimuli, contributing to averaging and WTA strategies.

Optogenetic activation of excitatory NI cells leads to predominantly WTA dynamics in the tectum

We next wanted to find out how optogenetic manipulation of the NI affects tectal dynamics. We combined multiplane functional imaging and cell-resolution optogenetic perturbations with two-photon computer-generated holographic (2P-CGH) photostimulation (Dal Maschio et al., 2017; Figure 5A). In the absence of visual stimulation, optogenetic activation of ChR2-expressing *lhx9*-positive neurons in the NI induced activity in the tectum that resembled WTA (one tectum with more cells being active, opto-activation index less than -0.25 or more than 0.25) and averaging dynamics (both tecta with almost equal numbers of active cells, opto-activation index between -0.25 and 0.25) (Figures 5B–5E). Detectable calcium signals in tectal cells after unilateral stimulation of *lhx9*-positive NI cells were evident in 9% of the trials, with the majority of successful trials leading to WTA dynamics (Figure 5B). Notably, our stimulation protocol resulted in stochastic tectal activity, with different cells in the tectum activated each time and left or right tectal activity dominating each trial. Such a variable response mirrors the behavior and suggests that, although the NI directly influences tectal activity, the effect may be mediated by a heterogeneous population interacting with the ipsilateral and contralateral tectum.

Next we wanted to find out how the NI contributes to tectal processing of looming visual stimuli. To investigate involvement of the NI in looming-evoked responses, we imaged activity in the NI and tectum in response to a single looming stimulus while optogenetically activating small subsets (8–10 cells) of excitatory *lhx9*-positive neurons in the NI (Figure 5F). This pairing of visual stimulation with photostimulation of the NI resulted in the

- (B) Probability that fish perform a swim bout in response to photostimulation under control (gray), ChR2+ (blue), and GtACR2+ (yellow) conditions. ChR2 and GtACR2 animals express ChR2-mCherry or GtACR2-YFP in excitatory *lhx9*-positive cells of the NI. Control animals express no optogenetic actuator.
(C) Probability that fish perform a swim bout when simultaneously presented with looming stimuli to each eye and the NI is stimulated unilaterally.
(D) Hierarchical clustering of swim bouts. Identified types are directional C-start escapes (blue), slow swims (green), and burst swims (red). Bottom: overlay of frames from representative bouts belonging to each of the three clusters.
(E) Tail beat frequency plotted against maximum tail amplitude for light-evoked bouts across all conditions. Density indicates the KDE over the maximum amplitude. Bouts evoked in ChR2+ fish (blue) are of lower amplitude compared with controls ($p = 0.043$, Kolmogorov-Smirnov test).
(F) Average number of burst swims evoked per trial in response to light stimulation across fish.
(G) As in (E) except for bouts evoked by presentation of equal looms to the two eyes during optogenetic stimulation. Distributions are not significantly different between control and optogenetic conditions ($p > 0.05$, Kolmogorov-Smirnov test).
(H) Average number of C-starts (WTA responses) evoked per trial in response to equal looms presented to the two eyes during simultaneous stimulation of the NI across fish.
Control fish, $n = 18$; ChR2+, $n = 21$; GtACR2+, $n = 9$.



(legend on next page)

modulation of tectal and NI neurons (Figures 5G and 5H). Interestingly, individual cells in the ipsilateral tectum increased or decreased their stimulus-evoked activity upon activation of the NI (Figures 5G, 5H, and S7A–S7F). Thus, the nature of the excitatory modulation of looming stimuli can be facilitatory and suppressive, providing further evidence for heterogeneity within the *lhx9*-positive NI population.

Ablation of specific NI cells disrupts behavioral responses to looming stimuli to both sides

We next tested the effects of ablating the NI on neural activity and behavior. Our optogenetics results suggest that such an experiment should disrupt responses to looming stimuli to both sides. Supporting this hypothesis, we observed that unilateral two-photon ablation of the GABAergic NI population with ultra-short laser pulses (Figure 6A) caused a deficit in looming-evoked escape responses to either side (Figures 6B and 6C). Similarly, animals with unilateral ablation of excitatory *lhx9*-positive NI neurons showed a significant reduction in escape responses (Figures 6D and 6E) compared with sham ablated animals (Figures S8A–S8D). Such a bilateral effect on escape responses from unilateral ablation is consistent with our optogenetic manipulations, which were unable to bias the directions of escapes in an acute manipulation (Figure 4G) and provides further evidence of a binocular computation implemented within the NI.

Hunting behavior, as measured by eye convergence, bout rate, and prey detection rate, was only mildly affected in NI-ablated fish (Figures S8G–S8L). J-turns, which fish use to orient toward prey that are lateral in the visual field, were intact after ablation of NI cells (Figures S8M–S8R). Optomotor response was intact by ablation of glutamatergic or GABAergic NI cells (Figures S8E and S8F). These controls indicate the specificity of the manipulation and suggest the existence of dedicated circuits for selecting stimuli of different valence.

NI cells are required to specifically activate looming responses in both tectal hemispheres

Next we imaged tectal cell activity (periventricular neurons) following ablation of NI cells. First we wanted to find out whether such treatment generally affected the processing of visual stimuli across tectal hemispheres. We stimulated one eye with a looming stimulus as well as with control stimuli, including prey and

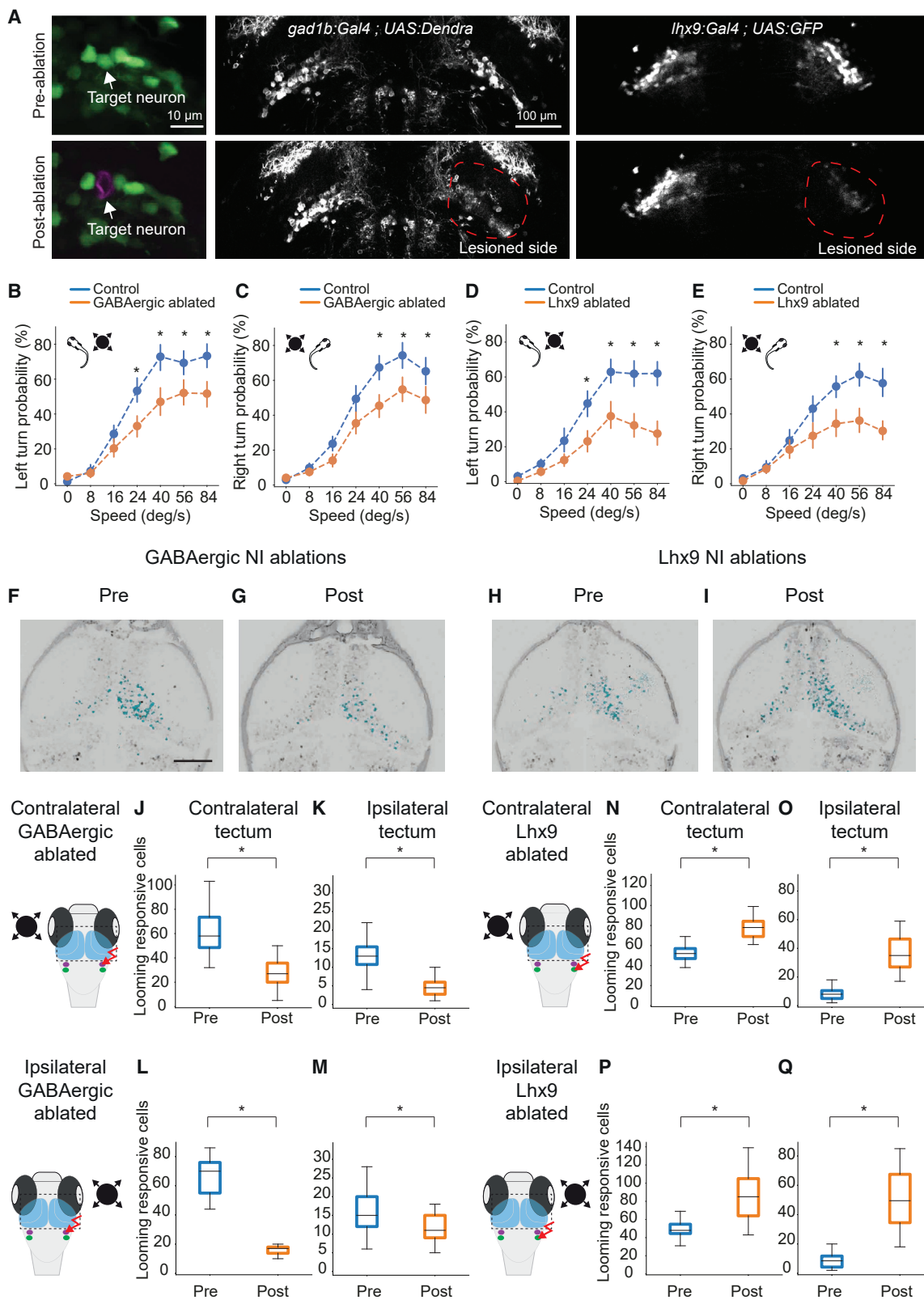
dimming. Unilateral ablation of GABAergic NI cells decreased looming responses in both tecta (Figures 6F, 6G, 6J, 6K, S9D, and S9E), whereas prey-like and dimming responses were unaffected (Figures S9L and S9M). These results match our observation that 90% of GABAergic-positive cells in the NI respond to looming stimuli and only a small percentage to prey-like (1%) and dimming (9%) stimuli (Figure S6D). We also observed a general decrease in the number of looming-responsive cells in both tecta during stimulation of the eye ipsilateral to the ablated NI (Figures 6L, 6M, S9H, and S9I). In contrast, ablation of *lhx9*-positive glutamatergic NI neurons bilaterally increased responses to looming (Figures 6H, 6I, 6N, 6O, S9F, and S9G) but not prey-like and dimming stimuli (Figures S9N and S9O), again matching the distribution of responsive cells (Figure S6A). Visual stimulation of the eye ipsilateral to the *lhx9* ablation also increased looming responsive cells in both tecta (Figures 6P, 6Q, S9J, and S9K). These results match the behavioral phenotypes we observed; unilateral ablation of excitatory or inhibitory NI neurons leads to bilateral and loom-specific deficits in neuronal responses, altering the weighted integration of visual stimuli across hemispheres, with concomitant bilateral effects on behavioral output. This modulation supports a role of the NI in binocular stimulus competition. Our data demonstrate involvement of NI cells in WTA and averaging dynamics and context-dependent functional connectivity between the NI and tectum.

Tecto-isthmic and isthmotectal projections form interhemispheric loops

To identify the neural circuit architecture underlying NI-mediated interhemispheric stimulus selection, we acquired a dataset of stochastically labeled, single-cell morphologies and co-registered these neurons in a standard brain atlas (Kunst et al., 2019). Co-alignment of tectal projection neurons (Helmbrecht et al., 2018) revealed that the axons of intertectal and tectobulbar neurons frequently innervate the neuropil regions of the NI (Figures 7A–7D and S10A–S10C). We noticed that, although tectobulbar axon collaterals appear to span the excitatory and inhibitory neuropil regions of the ipsilateral NI, intertectal neurons preferentially innervate the excitatory NI neuropil on both sides of the brain (Figures S10A–S10C). Thus, in the tecto-isthmic direction, there are neurons that project only ipsilaterally to the NI and extend to the hindbrain reticular formation

Figure 5. Optogenetic activation leads to WTA and averaging activity dynamics and modulates tectal responses to looming stimuli

- (A) Schematic of the holographic optogenetics experiment.
- (B) Opto-activation index. Unilateral optogenetic activation of *lhx9*-positive isthmic neurons (right side) leads to WTA and averaging activity in the tectum (in blue). The opto-activation index is calculated as follows: (responsive cells right tectum – responsive cells left tectum) / (responsive cells right tectum + responsive cells left tectum). Opto-index distribution for the control condition (ChR2 negative fish) is shown in gray. Distributions are significantly different ($p = 0.038$, two-sided Kolmogorov-Smirnov test).
- (C) Example of 10 cells from each tectum in a trial where the left tectum “won” (WTA). The black line shows mean response for all cells. Gray traces show individual cell activity.
- (D) Similar to (C) but for a trial where both tecta were equally active (averaging).
- (E) Similar to (C) and (D) but a trial where the right tectum “won” (WTA).
- (F) Activation of specific *lhx9*-positive isthmic neurons expressing Channelrhodopsin (ChR2; orange), combined with volumetric imaging of ipsilateral tectal responses (GCaMP6s, green). Up to five planes, including the tectum and NI region, were recorded simultaneously.
- (G) Photostimulation of *lhx9*-positive isthmic neurons. Some of the isthmic looming-evoked responses are unaffected by optogenetic stimulation (in gray), whereas others are either suppressed (magenta) or enhanced (green). Examples of averages of 10 cells are shown for each response type. Shaded areas represent SD.
- (H) Similar to (G) but for tectal cells.



(legend on next page)

as well as neurons that project bilaterally to the NI in both hemispheres.

To survey isthmotectal connections, we reconstructed single NI cells and traced their projections (Figures 7E–7H and S10E). We found bilateral projections from individual NI cells to both tecta. We identified three classes of glutamatergic neuronal projection types (Lhx9 classes I, II, and III). Excitatory neurons project to the ipsilateral and/or contralateral tectum and connect the two hemispheres via the postoptic commissure (Figures 7E and 7F). Lhx9 class I cells project first from the NI to the ipsilateral and then to the contralateral tectum (Figures 7E). We found class I cells that arborize mainly either in the ipsilateral or the contralateral side (Figure 7I). Lhx9 class II cells project first to the contralateral glutamatergic NI neuropil, with arborizations reaching the pretectum, thalamus, and a neuropil region close to the contralateral semicircular torus and tectum. These neurons then re-cross the midline and innervate the other hemisphere (Figures 7F and 7J). Lhx9 class III cells target only the ipsilateral thalamic region (Figure S10D).

We also identified two classes of GABAergic NI neurons (GABAergic classes I and II). GABAergic class I cells project to ipsilateral and contralateral tecta, crossing the midline via a dorsal commissure near the skin (Figure 7G). GABAergic class II cells project to the ipsilateral tectum only (Figure 7H). Our single-cell reconstructions reveal an intricate system of excitatory and inhibitory feedback loops that support interhemispheric computations.

Isthmotectal axon arborization patterns support focal excitation and broad inhibition

A common model of stimulus selection implementing WTA selection postulates the existence of localized enhancement of responses to a salient stimulus and widespread suppression of responses to background distractors. Consistent with this hypothesis, we found that glutamatergic NI neurons arborize

focally in the tectum (Figure S10F); their mean axonal innervation length in the tectum is 196 μm , with an average of 6 branches per arbor. GABAergic class II NI neuron arborization length in the tectum is also limited, with a mean length of 319 μm and on average of 18 branches per arbor. In contrast, arborizations of GABAergic class I NI neurons projecting to both tecta are, on average, five times larger than excitatory NI neurons: 969 μm in length and 39 branches per arbor ($p = 9.64 \times 10^{-4}$ for length and $p = 3.08 \times 10^{-3}$ for number of branches; Figure S10G). The layout of the isthmotectal system thus fulfills the predictions of the local enhancement/global suppression model of WTA dynamics across both hemispheres.

DISCUSSION

An animal's ability to respond to a single stimulus in a crowded visual scene is an ancestral form of selective attention (Krauzlis et al., 2018). In bottom-up, stimulus-driven attention, the saliency of a stimulus is compared with that of other stimuli in the scene, producing targeted behavioral responses. Determining the behavioral strategies, neurophysiological dynamics, as well as circuit motifs that mediate stimulus selection is key to understanding how animals allocate attentional resources and make behavioral decisions. Here we find evidence of stimulus selection in retinotectal and isthmotectal circuits. Our results support a model in which retinotectal circuits underlie monocular stimulus selection, whereas a newly discovered isthmotectal loop mediates binocular competition. Our findings are summarized schematically in Figure 8.

Stimulus selection is already evident from behavioral observations. When freely swimming fish encounter two looming disks, each able to trigger an escape response on its own, they escape from one randomly chosen stimulus in the majority of cases. In the remaining trials, the fish appear to average the locations of

Figure 6. Unilateral ablation of NI cells modulates looming-evoked responses bilaterally

(A) 2P laser ablation of isthmic neurons. Shown is an example of single cell ablation (left panels). After ablation of a cell, red fluorescence (magenta) is visible in the target spot. The center panels show representative images of unilateral 2P laser ablation of GABAergic-positive isthmic neurons in *gad1b:Gal4VP16^{mpn155}; UAS:Dendra-kras^{s1998t}* pre-ablation and post-ablation. Right panels: ablation of glutamatergic isthmic neurons in *lhx9:Gal4VP16^{mpn203}; UAS:EGFP* pre-ablation and post-ablation.

(B) Probability of left escapes in control (blue) and GABAergic NI-ablated fish (orange).

(C) Similar to (B) but for right escapes.

(D) Probability of left escapes in control (blue) and *lhx9* NI-ablated fish (orange).

(E) Similar to (D) but for right escapes. For all looming-evoked escape panels, error bars represent SD. $n = 12$ for control fish (blue). $n = 15$ for ablated fish (orange). * $p < 0.05$, Tukey's honestly significant difference (HSD) test.

(F and G) Example of the effect of unilateral ablation of the GABAergic-positive NI on the right hemisphere. (F) is before ablation and (G) is after ablation. The corresponding *t*-statistic for each pixel is calculated for looming-responsive cells and labeled in cyan.

(H and I) Example of the effect of unilateral ablation of the *lhx9*-positive NI on the right hemisphere before (H) and after (I) ablation.

(J) Number of looming-responsive cells in the contralateral (relative to looming stimulus) tectum before and after ablation of GABAergic-positive NI cells in the right hemisphere. $n = 4$.

(K) Number of looming-responsive cells in the ipsilateral (relative to looming stimulus) tectum.

(L) Number of looming responsive cells in the contralateral tectum (relative to looming stimulus) for the intact hemisphere before and after ablation of GABAergic-positive NI cells in the right hemisphere. $N = 2$.

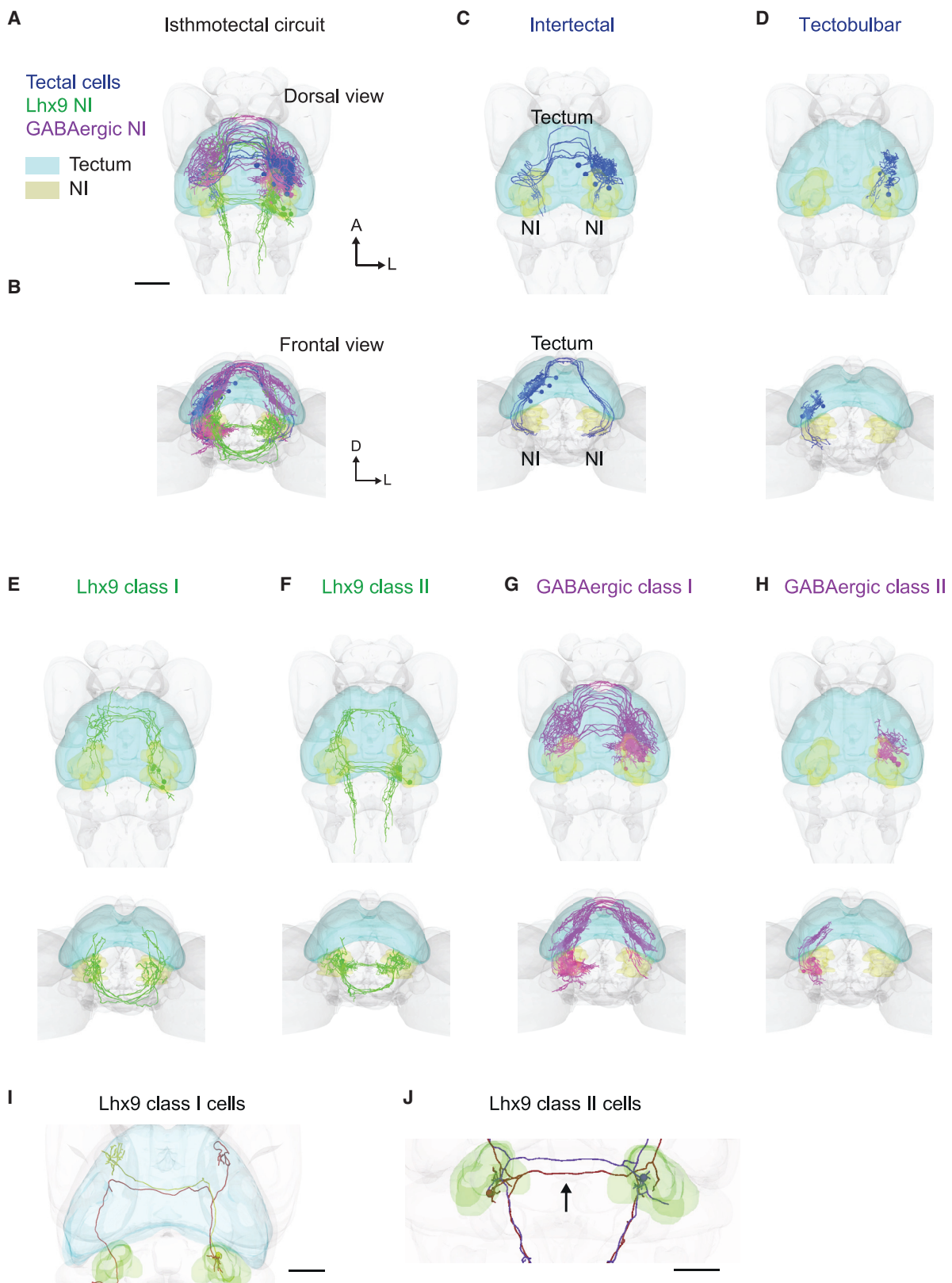
(M) Number of looming-responsive cells in the ipsilateral tectum (relative to looming stimulus) for the intact hemisphere after ablation of the GABAergic-positive NI.

(N) Number of looming-responsive cells in the contralateral (relative to looming stimulus) tectum before and after ablation of *lhx9*-positive NI cells in the right hemisphere. $n = 3$ fish.

(O) Number of looming-responsive cells in the ipsilateral (relative to looming stimulus) tectum.

(P) Number of looming-responsive cells in the contralateral tectum (relative to looming stimulus) for the intact hemisphere before and after ablation of *lhx9*-positive NI cells in the right hemisphere. $n = 2$ fish.

(Q) Number of looming-responsive cells in the ipsilateral tectum (relative to looming stimulus) for the intact hemisphere after ablation of *lhx9*-positive NI cells. For all panels, * $p < 0.05$, Mann-Whitney *U* test.



(legend on next page)

the two stimuli and swim between them. Individual animals employ either strategy in successive trials, suggesting that WTA and averaging can occur in the same brain. Their respective engagement presumably depends on stimulus history and internal state. When the two stimuli are unequal in expansion rate, the escape responses are biased to the stronger stimulus, indicating that zebrafish larvae weigh the relative saliences of competing stimuli. This behavioral choice exhibited by larval zebrafish thus shows the hallmarks of selective spatial attention.

Neural signatures of WTA first emerge in the early stages of visual processing: the retina and the tectum. Interestingly, we found that a salient stimulus suppresses the response to the weaker stimulus presented to the same eye already at the level of the RGCs (Figures 2 and 8A). By chemogenetic ablation of the tectum, we ruled out that this effect is the result of feedback modulation of RGC presynaptic axon terminals by tectal cells. Presentation of two prey-like objects produced the same WTA dynamics in the retinotectal system, suggesting that such dynamics are part of a global mechanism involved in stimulus selection in diverse behavioral contexts (escape and hunting) and independent of stimulus valence. Monocular stimulus competition is likely the result of antagonistic mechanisms within the inner retina, apparently operating outside of the classical receptive field (Deny et al., 2017; McIlwain, 1964).

Retinal mechanisms cannot, in principle, account for competition across the hemispheres. We discovered that the NI, together with the tectum, integrates information from both eyes. A reciprocal loop between these two structures may enhance responses to the stronger stimulus and suppress responses to the weaker stimulus. As a result, the two tecta show unbalanced activity patterns in response to looming disks presented to opposite sides (Figures 3 and 8B). Inter-hemispheric inhibition has been demonstrated in other species and contexts. In *Drosophila*, cats, barn owls, and monkeys, for example, a strong stimulus located anywhere outside of the receptive field, including in the opposite hemisphere, can suppress responses to an otherwise effective stimulus (Herman et al., 2018; Mysore and Knudsen, 2012; Rizzolatti et al., 1979; Sun et al., 2017).

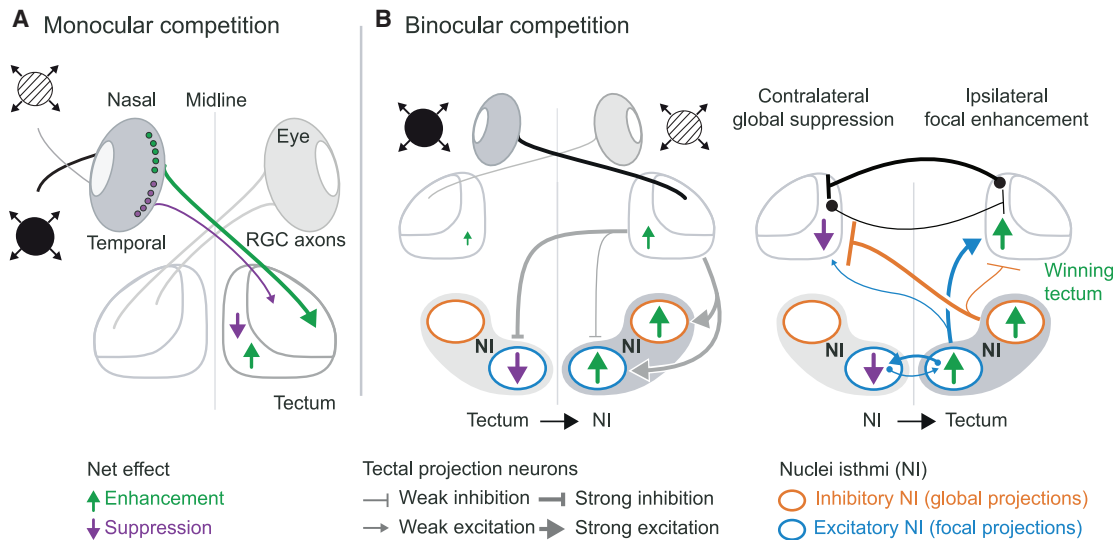
Our data support a mechanism where neuronal projection patterns and transmitter identities of recurrent isthmotectal connections lead to focal enhancement of the most salient stimulus combined with global suppression elsewhere (Brandt and Wessel, 2007; Cisek, 2019; Jovanic et al., 2016; Koyama and Pujala,

2018; Mysore and Knudsen, 2012). This neural circuit possesses four key properties. First, the relative levels of tectal and isthmic activity in the right and left hemispheres can discriminate the stronger stimulus. Depending on which side of the brain “wins,” neurons exhibit switch-like behavior, as expected from a WTA mechanism across hemispheres. Second, by virtue of their bilateral projections, NI neurons can enhance or suppress tectal cell activity in response to looming stimuli across both hemispheres. Third, excitatory NI cells arborize focally, whereas inhibitory NI cells arborize broadly. Fourth, unilateral manipulation of the NI causes bilateral effects in tectal neural dynamics and behavior. These results suggest that WTA dynamics emerge from a tightly coordinated interhemispheric computation. We argue that salient stimuli are detected based on the relative levels of activity in the right and left tectum, similar to a pooling model (Herman et al., 2018). We postulate that Lhx9 class I cells may implement WTA (directed escapes) by driving more activity in the ipsilateral or contralateral tectum together with global inhibition of the “losing” side provided by GABAergic NI cells. Lhx9 class II cells are potential candidates for involvement in implementation of an averaging strategy (leading to burst forward movements), with direct contralateral projections to the other NI leading to a balancing of activity across hemispheres, preventing one side from “winning” during stimulus competition.

The isthmotectal system is at least as old as the osteichthyan lineage, which includes bony fish, amphibians, mammals, and sauropsids. The NI’s possible behavioral functions have been debated over the years and may not be restricted to prioritization of threats. We show here that unilateral manipulation of NI cells causes bilateral behavioral impairments in response to looming stimuli and deficits in visual processing on both sides of the brain. In contrast, ablation of cholinergic NI neurons in zebrafish causes deficits in hunting but only mild effects in loom avoidance (Henriques et al., 2019). Moreover, a population of GABAergic neurons, ventral to the tectum and in close apposition to the NI, projects to both tecta and is involved in interhemispheric coordination for prey capture (Gebhardt et al., 2019). We propose that the NI, perhaps in concert with other tegmental and peri-isthmic nuclei, has multiple region-specific functions. Accordingly, our work here and the aforementioned studies may have investigated distinct subpopulations of isthmic neurons. There is precedent for such functional segregation by stimulus valence. Processing of prey versus looming information, for example, is confined to separate layers of the tectum (Semmelhack et al.,

Figure 7. Cellular architecture of isthmotectal circuitry

- (A) Cellular-resolution atlas of isthmotectal circuitry showing single-cell reconstructions. Shown are tectal cells in blue, *Lhx9*-positive NI cells in green, and GABAergic-positive NI cells in magenta, dorsal view, and masks for the tectum and NI (light blue and yellow, respectively).
- (B) Same as (A) but frontal view.
- (C) Intertectal cells with a bifurcated axon, terminating in the vicinity of the NI on both sides.
- (D) Tectobulbar neurons targeting the ipsilateral NI.
- (E) *Lhx9*-positive NI cells (class I) projecting first to the ipsilateral tectum and then to the contralateral tectum.
- (F) *Lhx9*-positive NI cells (class II) projecting first to the contralateral NI, close to the contralateral tectum, and then to the ipsilateral tectum.
- (G) GABAergic-positive NI cells (class I) projecting first to the ipsilateral tectum and then to the contralateral tectum.
- (H) GABAergic-positive NI cells (class II) projecting only to the ipsilateral tectum. For each morphological type, dorsal and frontal views are shown.
- (I) Example of two *Lhx9* class I cells with projections to the tectum. Both cell bodies are on the right. The brown cell shows terminations mainly in the ipsilateral tectum, whereas the green cell shows termination mainly in the contralateral tectum.
- (J) Example of reciprocal projections of two *Lhx9* class II NI cells. The red cell has its soma in the left NI and terminations in the right NI. The purple cell has its soma in the right NI and terminations in the left NI. Both cells have descending projections to the hindbrain. Scale bars, 50 μ m.

**Figure 8. Schematic summary of findings**

(A) Schematized summary of findings for monocular competition. The most salient stimulus “wins” in the retina through reciprocal inhibition, possibly mediated by amacrine cells. Saliency tuning is sharpened by a tectum-intrinsic circuit.

(B) Circuit model for binocular competition. Each tectum drives activity in the ipsilateral NI (putative excitatory tectobulbar neurons) and suppresses activity in the contralateral NI (putative inhibitory intertectal neurons). Focal enhancement, mediated by excitatory NI cells, is stronger on the “winning” stimulus side (green arrows). Suppression, mediated by globally projecting inhibitory NI neurons, is stronger on the “losing” stimulus side (magenta arrows). Reciprocal isthmotectal loops ensure focal enhancement of responses to a stronger stimulus and suppression of responses to a weaker stimulus, implementing a WTA computation. Black connections across both tecta represent putative inhibitory commissural neurons projecting to the contralateral side. Equal activity in both NIs may result in neither tectum winning and an averaging strategy being implemented instead.

2014; Temizer et al., 2015) and transmitted by separate output pathways to the tegmentum and reticular formation (Helmbrecht et al., 2018).

We conclude that a feedforward retinotectal and a recurrent isthmotectal circuit implement context-dependent target selection and may form the basis of an evolutionarily conserved, bottom-up attention mechanism. It will be important to examine how the choice between escape, other defensive actions (e.g., freezing), and prey capture is computed as a function of the type of stimuli and their combination. Future work will help clarify interactions between different subpopulations of NI neurons. Further dissection of these interconnected circuits, especially under the top-down influence of the animal’s internal state, such as experience, hunger, or stress, will reveal elementary principles underlying selective spatial attention in vertebrates.

STAR★METHODS

Detailed methods are provided in the online version of this paper and include the following:

- KEY RESOURCES TABLE
- RESOURCE AVAILABILITY
 - Lead contact
 - Materials availability
 - Data and code availability
- EXPERIMENTAL MODEL AND SUBJECT DETAILS
 - Zebrafish lines

- Q-system transgenics
- METHOD DETAILS
 - Visual competition behavioral assay
 - Data analysis for behavioral experiments with competing looming stimuli
 - Modeling
 - Prey capture experiments
 - Calcium imaging
 - Two-photon computer generated holographic (2P-CGH) optogenetics
 - Genetic ablation of neurons
 - Imaging analysis
 - Optogenetic stimulation during presentation of looming stimuli
 - Analysis of optogenetic experiments
 - Two-photon ablation of neurons
 - Single-cell reconstructions
 - Confocal imaging and anatomical reconstruction of neurons
 - *In situ* hybridization and immunohistochemistry
- QUANTIFICATION AND STATISTICAL ANALYSIS
 - Quantification of arbor length and number of arborizations of NI cells

SUPPLEMENTAL INFORMATION

Supplemental Information can be found online at <https://doi.org/10.1016/j.neuron.2020.12.002>.

ACKNOWLEDGMENTS

We thank Yunmin Wu, Aristides Arrenberg, and Ruben Portugues for advice. Anna Kramer helped with drawing **Figure 8**. Enrico Kühn, Styliani Koutsouli, Krasimir Slanchev, and Irene Arnold-Ammer provided expert technical support. Vilim Štih and Andreas Kist shared scripts used in the analysis of imaging data. Wolfgang Driever provided the riboprobes for detection of *gad1b* and *trh*. Michael Kunst and Nawwar Mokayes assisted with experiments and analysis of anatomical reconstruction data. We thank all members of the Baier lab for discussions. Funding was provided by the Max Planck Society and the DFG (SFB 870 “Assembly and Function of Neural Circuits” and the Priority Program SPP 1926 “Next Generation Optogenetics” to H.B.). K.K. received support from NIG-JOINT (2014-A) and the Japan Agency for Medical Research and Development (JP20km0210087 and JP20km0210168).

AUTHOR CONTRIBUTIONS

Conceptualization, A.M.F. and H.B.; Methodology, A.M.F., J.L., J.C.D., T.O.H., D.S.M., Y.K., E.L., K.K., and M.D.M.; Software, A.M.F., J.L., J.C.D., T.O.H., D.S.M., and M.D.M.; Formal Analysis, A.M.F., J.L., J.C.D., T.O.H., D.S.M., and M.D.M.; Investigation, A.M.F., D.S.M., E.L., and M.D.M.; Writing – Original Draft, A.M.F. and H.B.; Writing – Review & Editing, all authors; Funding Acquisition, H.B.; Supervision, H.B.

DECLARATION OF INTERESTS

The authors declare no competing interests.

Received: June 15, 2020

Revised: November 9, 2020

Accepted: December 2, 2020

Published: December 22, 2020

REFERENCES

- Arrenberg, A.B., Del Bene, F., and Baier, H. (2009). Optical control of zebrafish behavior with halorhodopsin. *Proc. Natl. Acad. Sci. USA* **106**, 17968–17973.
- Asakawa, K., Suster, M.L., Mizusawa, K., Nagayoshi, S., Kotani, T., Urasaki, A., Kishimoto, Y., Hibi, M., and Kawakami, K. (2008). Genetic dissection of neural circuits by Tol2 transposon-mediated Gal4 gene and enhancer trapping in zebrafish. *Proc. Natl. Acad. Sci. USA* **105**, 1255–1260.
- Ben-Tov, M., Donchin, O., Ben-Shahar, O., and Segev, R. (2015). Pop-out in visual search of moving targets in the archer fish. *Nat. Commun.* **6**, 6476.
- Berens, P. (2009). CircStat: A MATLAB Toolbox for Circular Statistics. *Journal of Statistical Software* **31**, 1–21.
- Bhattacharyya, K., McLean, D.L., and MacIver, M.A. (2017). Visual Threat Assessment and Reticulospinal Encoding of Calibrated Responses in Larval Zebrafish. *Curr. Biol.* **27**, 2751–2762.e6.
- Bianco, I.H., Kampff, A.R., and Engert, F. (2011). Prey capture behavior evoked by simple visual stimuli in larval zebrafish. *Front. Syst. Neurosci.* **5**, 101.
- Brandt, S.F., and Wessel, R. (2007). Winner-take-all selection in a neural system with delayed feedback. *Biol. Cybern.* **97**, 221–228.
- Budick, S.A., and O’Malley, D.M. (2000). Locomotor repertoire of the larval zebrafish: swimming, turning and prey capture. *J. Exp. Biol.* **203**, 2565–2579.
- Burgess, H.A., and Granato, M. (2007). Modulation of locomotor activity in larval zebrafish during light adaptation. *J. Exp. Biol.* **210**, 2526–2539.
- Cisek, P. (2007). Cortical mechanisms of action selection: the affordance competition hypothesis. *Philos. Trans. R. Soc. Lond. B Biol. Sci.* **362**, 1585–1599.
- Cisek, P. (2019). Resynthesizing behavior through phylogenetic refinement. *Atten. Percept. Psychophys.* **81**, 2265–2287.
- Dal Maschio, M., Donovan, J.C., Helmbrecht, T.O., and Baier, H. (2017). Linking Neurons to Network Function and Behavior by Two-Photon Holographic Optogenetics and Volumetric Imaging. *Neuron* **94**, 774–789.e5.
- Davison, J.M., Akitake, C.M., Goll, M.G., Rhee, J.M., Gosse, N., Baier, H., Halpern, M.E., Leach, S.D., and Parsons, M.J. (2007). Transactivation from Gal4-VP16 transgenic insertions for tissue-specific cell labeling and ablation in zebrafish. *Dev. Biol.* **304**, 811–824.
- Del Bene, F., Wyart, C., Robles, E., Tran, A., Looger, L., Scott, E.K., Isacoff, E.Y., and Baier, H. (2010). Filtering of visual information in the tectum by an identified neural circuit. *Science* **330**, 669–673.
- Deny, S., Ferrari, U., Macé, E., Yger, P., Caplette, R., Picaud, S., Tkačik, G., and Marre, O. (2017). Multiplexed computations in retinal ganglion cells of a single type. *Nat. Commun.* **8**, 1964.
- Dunn, T.W., Gebhardt, C., Naumann, E.A., Riegler, C., Ahrens, M.B., Engert, F., and Del Bene, F. (2016). Neural Circuits Underlying Visually Evoked Escapes in Larval Zebrafish. *Neuron* **89**, 613–628.
- Ewert, J.-P. (1997). Neural correlates of key stimulus and releasing mechanism: a case study and two concepts. *Trends Neurosci.* **8**, 332–339.
- Feng, L., Zhao, T., and Kim, J. (2015). NeuTube 1.0: A New Design for Efficient Neuron Reconstruction Software Based on the SWC Format. *eNeuro* **2**.
- Fernandes, A.M., Fero, K., Arrenberg, A.B., Bergeron, S.A., Driever, W., and Burgess, H.A. (2012). Deep brain photoreceptors control light seeking behavior in zebrafish larvae. *Curr. Biol.* **22**, 2042–2047.
- Förster, D., Arnold-Ammer, I., Laurell, E., Barker, A.J., Fernandes, A.M., Finger-Baier, K., Filosa, A., Helmbrecht, T.O., Kölsch, Y., Kühn, E., et al. (2017). Genetic targeting and anatomical registration of neuronal populations in the zebrafish brain with a new set of BAC transgenic tools. *Sci. Rep.* **7**, 5230.
- Gebhardt, C., Auer, T.O., Henriques, P.M., Rajan, G., Duroure, K., Bianco, I.H., and Del Bene, F. (2019). An interhemispheric neural circuit allowing binocular integration in the optic tectum. *Nat. Commun.* **10**, 5471.
- Gruberg, E., Dudkin, E., Wang, Y., Marín, G., Salas, C., Sentis, E., Letelier, J., Mpodozis, J., Malpeli, J., Cui, H., et al. (2006). Influencing and interpreting visual input: the role of a visual feedback system. *J. Neurosci.* **26**, 10368–10371.
- Heap, L.A.L., Vanwalleghem, G., Thompson, A.W., Favre-Bulle, I.A., and Scott, E.K. (2018). Luminance Changes Drive Directional Startle through a Thalamic Pathway. *Neuron* **99**, 293–301.e4.
- Helmbrecht, T.O., Dal Maschio, M., Donovan, J.C., Koutsouli, S., and Baier, H. (2018). Topography of a Visuomotor Transformation. *Neuron* **100**, 1429–1445.e4.
- Henley, J.M., Lindstrom, J.M., and Oswald, R.E. (1986). Acetylcholine receptor synthesis in retina and transport to optic tectum in goldfish. *Science* **232**, 1627–1629.
- Henriques, P.M., Rahman, N., Jackson, S.E., and Bianco, I.H. (2019). Nucleus Isthmi Is Required to Sustain Target Pursuit during Visually Guided Prey-Catching. *Curr. Biol.* **29**, 1771–1786.e5.
- Herman, J.P., Katz, L.N., and Krauzlis, R.J. (2018). Midbrain activity can explain perceptual decisions during an attention task. *Nat. Neurosci.* **21**, 1651–1655.
- Itti, L., and Koch, C. (2000). A saliency-based search mechanism for overt and covert shifts of visual attention. *Vision Res.* **40**, 1489–1506.
- Jovanic, T., Schneider-Mizell, C.M., Shao, M., Masson, J.-B., Denisov, G., Fetter, R.D., Mensh, B.D., Truman, J.W., Cardona, A., and Zlatic, M. (2016). Competitive Disinhibition Mediates Behavioral Choice and Sequences in Drosophila. *Cell* **167**, 858–870.e19.
- Kardamakis, A.A., Saitoh, K., and Grillner, S. (2015). Tectal microcircuit generating visual selection commands on gaze-controlling neurons. *Proc. Natl. Acad. Sci. USA* **112**, E1956–E1965.
- Klapoetke, N.C., Nern, A., Peek, M.Y., Rogers, E.M., Breads, P., Rubin, G.M., Reiser, M.B., and Card, G.M. (2017). Ultra-selective looming detection from radial motion opponency. *Nature* **551**, 237–241.
- Knudsen, E.I. (2018). Neural Circuits That Mediate Selective Attention: A Comparative Perspective. *Trends Neurosci.* **41**, 789–805.
- Koch, C., and Ullman, S. (1985). Shifts in selective visual attention: towards the underlying neural circuitry. *Hum. Neurobiol.* **4**, 219–227.

- Koyama, M., and Pujala, A. (2018). Mutual inhibition of lateral inhibition: a network motif for an elementary computation in the brain. *Curr. Opin. Neurobiol.* 49, 69–74.
- Krauzlis, R.J., Bogadhi, A.R., Herman, J.P., and Bollimunta, A. (2018). Selective attention without a neocortex. *Cortex* 102, 161–175.
- Kunst, M., Laurell, E., Mokayes, N., Kramer, A., Kubo, F., Fernandes, A.M., Förster, D., Dal Maschio, M., and Baier, H. (2019). A Cellular-Resolution Atlas of the Larval Zebrafish Brain. *Neuron* 103, 21–38.e5.
- Larsch, J., and Baier, H. (2018). Biological Motion as an Innate Perceptual Mechanism Driving Social Affiliation. *Curr. Biol.* 28, 3523–3532.e4.
- Lee, D.K., Itti, L., Koch, C., and Braun, J. (1999). Attention activates winner-take-all competition among visual filters. *Nat. Neurosci.* 2, 375–381.
- Lisberger, S.G., and Ferrara, V.P. (1997). Vector averaging for smooth pursuit eye movements initiated by two moving targets in monkeys. *J. Neurosci.* 17, 7490–7502.
- Löhr, H., Ryu, S., and Driever, W. (2009). Zebrafish diencephalic A11-related dopaminergic neurons share a conserved transcriptional network with neuroendocrine cell lineages. *Development* 136, 1007–1017.
- Lopes, G., Bonacchi, N., Frazão, J., Neto, J.P., Atallah, B.V., Soares, S., Moreira, L., Matias, S., Itskov, P.M., Correia, P.A., et al. (2015). Bonsai: an event-based framework for processing and controlling data streams. *Front. Neuroinform.* 9, 7.
- Marques, J.C., Lackner, S., Félix, R., and Orger, M.B. (2018). Structure of the Zebrafish Locomotor Repertoire Revealed with Unsupervised Behavioral Clustering. *Curr. Biol.* 28, 181–195.e5.
- McIlwain, J.T. (1964). Receptive fields of optic tract axons and lateral geniculate cells: peripheral extent and barbiturate sensitivity. *J. Neurophysiol.* 27, 1154–1173.
- Mearns, D.S., Donovan, J.C., Fernandes, A.M., Semmelhack, J.L., and Baier, H. (2020). Deconstructing Hunting Behavior Reveals a Tightly Coupled Stimulus-Response Loop. *Curr. Biol.* 30, 54–69.e9.
- Miri, A., Daie, K., Burdine, R.D., Aksay, E., and Tank, D.W. (2011). Regression-Based Identification of Behavior-Encoding Neurons During Large-Scale Optical Imaging of Neural Activity at Cellular Resolution. *J. Neurophysiol.* 105, 964–980.
- Mohamed, G.A., Cheng, R.-K., Ho, J., Krishnan, S., Mohammad, F., Claridge-Chang, A., and Jesuthasan, S. (2017). Optical inhibition of larval zebrafish behaviour with anion channelrhodopsins. *BMC Biol.* 15, 103.
- Mysore, S.P., and Knudsen, E.I. (2012). Reciprocal inhibition of inhibition: a circuit motif for flexible categorization in stimulus selection. *Neuron* 73, 193–205.
- Northmore, D.P. (1991). Visual responses of nucleus isthmi in a teleost fish (*Lepomis macrochirus*). *Vision Res.* 31, 525–535.
- Northmore, D.P.M., and Gallagher, S.P. (2003). Functional relationship between nucleus isthmi and tectum in teleosts: synchrony but no topography. *Vis. Neurosci.* 20, 335–348.
- Nummela, S.U., and Krauzlis, R.J. (2011). Superior colliculus inactivation alters the weighted integration of visual stimuli. *J. Neurosci.* 31, 8059–8066.
- Ottes, F.P., Van Gisbergen, J.A., and Eggermont, J.J. (1984). Metrics of saccade responses to visual double stimuli: two different modes. *Vision Res.* 24, 1169–1179.
- Peirce, J., Gray, J.R., Simpson, S., MacAskill, M., Höchenberger, R., Sogo, H., Kastman, E., and Lindeløv, J.K. (2019). PsychoPy2: Experiments in behavior made easy. *Behav. Res. Methods* 51, 195–203.
- Potter, C.J., Tasic, B., Russler, E.V., Liang, L., and Luo, L. (2010). The Q System: A Repressible Binary System for Transgene Expression, Lineage Tracing and Mosaic Analysis. *Cell* 141, 536–548.
- Riabinina, O., Luginbuhl, D., Marr, E., Liu, S., Wu, M.N., Luo, L., and Potter, C.J. (2015). Improved and expanded Q-system reagents for genetic manipulations. *Nat. Methods* 12, 219–222, 5 p following 222.
- Rizzolatti, G., Bertoni, G., and Buchtel, H.A. (1979). Interference of concomitant motor and verbal tasks on simple reaction time: a hemispheric difference. *Neuropsychologia* 17, 323–330.
- Robles, E., Filosa, A., and Baier, H. (2013). Precise Lamination of Retinal Axons Generates Multiple Parallel Input Pathways in the Tectum. *J. Neurosci.* 33, 5027–5039.
- Rohlfing, T., and Maurer, C.R. (2003). Nonrigid image registration in shared-memory multiprocessor environments with application to brains, breasts, and bees. *IEEE Trans. Inf. Technol. Biomed.* 7, 16–25.
- Sareen, P., Wolf, R., and Heisenberg, M. (2011). Attracting the attention of a fly. *Proc. Natl. Acad. Sci. USA* 108, 7230–7235.
- Sato, T., Sato, F., Kamezaki, A., Sakaguchi, K., Tanigome, R., Kawakami, K., and Sehara-Fujisawa, A. (2015). Neuregulin 1 Type II-ErbB Signaling Promotes Cell Divisions Generating Neurons from Neural Progenitor Cells in the Developing Zebrafish Brain. *PLoS ONE* 10, e0127360.
- Satou, C., Kimura, Y., Hirata, H., Suster, M.L., Kawakami, K., and Higashijima, S. (2013). Transgenic tools to characterize neuronal properties of discrete populations of zebrafish neurons. *Development* 140, 3927–3931.
- Schellart, N.A.M., Riemsdag, F.C.C., and Sperkreijse, H. (1979). Center-surround organisation and interactions in receptive fields of goldfish tectal units. *Vision Res.* 19, 459–467.
- Semmelhack, J.L., Donovan, J.C., Thiele, T.R., Kuehn, E., Laurell, E., and Baier, H. (2014). A dedicated visual pathway for prey detection in larval zebrafish. *eLife* 3, 3.
- Sun, Y., Nern, A., Franconville, R., Dana, H., Schreiter, E.R., Looger, L.L., Svoboda, K., Kim, D.S., Hermundstad, A.M., and Jayaraman, V. (2017). Neural signatures of dynamic stimulus selection in *Drosophila*. *Nat. Neurosci.* 20, 1104–1113.
- Tabor, K.M., Bergeron, S.A., Horstick, E.J., Jordan, D.C., Aho, V., Porkka-Heiskanen, T., Haspel, G., and Burgess, H.A. (2014). Direct activation of the Mauthner cell by electric field pulses drives ultrarapid escape responses. *J. Neurophysiol.* 112, 834–844.
- Temizer, I., Donovan, J.C., Baier, H., and Semmelhack, J.L. (2015). A Visual Pathway for Looming-Evoked Escape in Larval Zebrafish. *Curr. Biol.* 25, 1823–1834.
- Thiele, T.R., Donovan, J.C., and Baier, H. (2014). Descending control of swim posture by a midbrain nucleus in zebrafish. *Neuron* 83, 679–691.
- Volkmann, K., Chen, Y.-Y., Harris, M.P., Wullimann, M.F., and Köster, R.W. (2010). The zebrafish cerebellar upper rhombic lip generates tegmental hindbrain nuclei by long-distance migration in an evolutionary conserved manner. *J. Comp. Neurol.* 518, 2794–2817.
- Wang, L., and Krauzlis, R.J. (2018). Visual Selective Attention in Mice. *Curr. Biol.* 28, 676–685.e4.
- Zhaoping, L. (2016). From the optic tectum to the primary visual cortex: migration through evolution of the saliency map for exogenous attentional guidance. *Curr. Opin. Neurobiol.* 40, 94–102.

STAR★METHODS

KEY RESOURCES TABLE

REAGENT or RESOURCE	SOURCE	IDENTIFIER
Antibodies		
Mouse anti-TH	Merck Millipore	RRID:AB_2201528
Mouse anti-REELIN	Millipore	RRID:AB_10682217
Mouse anti-GFP	Takara Bio Clontech	RRID:AB_10013427
Chicken anti-GFP	Thermo Fisher Scientific	RRID:AB_2534023
Goat anti-CHAT	Merck Millipore	RRID:AB_2079751
Chemicals, Peptides, and Recombinant Proteins		
DAPI	Sigma-Aldrich	28718-90-3
Metronidazole	Sigma-Aldrich	M3761
Experimental Models: Organisms/Strains		
Tg(ath5:QF2)mpn405	This manuscript	N/A
Tg(QUAS:GFPcaax)mpn163	This manuscript	N/A
Tg(QUAS:GCaMP6s)mpn164	This manuscript	N/A
Tg(QUAS:epNTR-tagRFP)mpn165	This manuscript	N/A
Tg(UAS:HaloTagCAAX)mpn170	This manuscript	N/A
Tg(elavl3:lyn-tagRFP)mpn404	Dal Maschio et al., 2017	ZDB-ALT-170731-38
Tg(UAS:ChR2(H134R)-mCherry)mpn134	Dal Maschio et al., 2017	ZDB-ALT-170731-36
Tg(UAS:GtACR2-eYFP)sq212	Mohamed et al., 2017	ZDB-ALT-170913-6
Tg(elavl3:nlsGCaMP6s)mpn400	Dal Maschio et al., 2017	ZDB-ALT-170731-37
Tg(gad1b:Gal4VP16)mpn155	Förster et al., 2017	ZDB-ALT-160726-5
Tg(lhx9:Gal4VP16)mpn203	Förster et al., 2017	ZDB-ALT-170908-16
Tg(chata:Gal4VP16)mpn202	Förster et al., 2017	ZDB-ALT-170908-4
Tg(nkSAGFFL81C)	Sato et al., 2015	ZDB-ALT-151006-4
Tg(UAS:nfsb-mCherry)c264	Davison et al., 2007	ZDB-ALT-070316-1
Tg(–7atoh7:GAL4-VP16)s1992tTg	Del Bene et al., 2010	ZDB-ALT-110912-2
Tg(gad1b: loxP-DsRed-loxP-GFP)	Satou et al., 2013	ZDB-TGCONSTRCT-131127-7
Tg(vglut2a:loxP-DsRedloxP-GFP)	Satou et al., 2013	ZDB-TGCONSTRCT-110413-4
Tg(UAS:GCaMP6s)mpn101	Thiele et al., 2014	ZDB-ALT-140811-3
Tg(UAS:Dendra-kras)s1998t	Arrenberg et al., 2009	ZDB-ALT-110808-3
Tg(elavl3:GCaMP6s)a13203	Dunn et al., 2016	ZDB-ALT-180502-2
Tg(UAS:Dendra-kras)s1998t	Arrenberg et al., 2009	ZDB-ALT-110808-3
Tg(5xUAS:EGFP)zf82	Asakawa et al., 2008	ZDB-ALT-080528-1
Tg(UAS-E1b:Kaede)s1999t	Davison et al., 2007	ZDB-TGCONSTRCT-070314-1
Software and Algorithms		
Python 2.7	Python	https://www.python.org/
Python 3.7	Python	https://www.python.org/
CMTK	Rohlfing and Maurer, 2003	https://www.nitrc.org/projects/cmtk/
Fiji (ImageJ)	NIH	http://fiji.sc/
Psychopy2	Peirce et al., 2019	https://www.psychopy.org/
neuTube	Feng et al., 2015	https://www.neutracing.com/

RESOURCE AVAILABILITY

Lead contact

Further information and requests for reagents should be directed to and will be fulfilled by the Lead Contact, Herwig Baier (hbaier@neuro.mpg.de).

Materials availability

Unique materials such as plasmids generated in this study will be available upon request without any restrictions.

Data and code availability

The datasets and custom software that support the findings of this study will be made available upon request.

EXPERIMENTAL MODEL AND SUBJECT DETAILS

All animal procedures conformed to the institutional guidelines set by the Max Planck Society and were approved under licenses from the regional government of Upper Bavaria (Regierung von Oberbayern).

Zebrafish lines

For the experiments in this study, we used 5–9 days post fertilization (d.p.f.) larvae carrying mutations in the *mitfa* allele (nacre). Sex is not determined at larval stage. Fish were raised on a 14h light/ 10h dark cycle at 28°C. Transgenic lines used in this study are shown in the Key Resources Table. For making the *Tg(UAS:HalotagCAAX)mpn170* line, the pFC14A HaloTag CMV Flexi Vector was purchased from Promega and the HaloTag was inserted with an N-terminal CAAX domain into a pTol2 UAS vector with bleeding heart marker at the EcoRI site. This construct was pressure-injected together with Tol2 mRNA (concentration for both: 25 ng/l) into one- to two-cell-stage embryos. Positive carriers of the construct were raised until adulthood and crossed to the *Tg(gad1b:Gal4VP16)mpn155* line. 1 μM of Halotag ligand (JF549, kind gift of Luke Levis, Janelia) and 1:500 dilution of lysotracker (deep red, Invitrogen, L12492) in DMSO (final concentration 1%), were added to the water of 4 dpf larvae. The larvae were kept in this solution for 36 h. Dyes were washed out prior to imaging at 6 dpf.

Q-system transgenics

A pTol2-(5x)QUAS-e1b:EcoRV-polyA;cmlc2:mCherry vector was generated using oligo synthesized QUAS promoter sequences (Potter et al., 2010). A GCaMP6s fragment (Thiele et al., 2014) was inserted into the EcoRV-linearized vector using traditional restriction-ligation cloning. The same approach was used to generate an epNTR-TagRFP (Tabor et al., 2014) and GFPcaax (Förster et al., 2017) version. To generate the *Tg(QUAS)* reporter lines, transposase mRNA (50 ng/μl) and the construct (25 ng/μl) were co-injected into TL/nacre zebrafish eggs. Injected fish were sorted based on heart expression of the transgenesis marker cmlc2:mCherry and raised into adulthood. Founders were obtained by outcrosses to TL/nacre. The QF2 coding sequence was obtained from Addgene Plasmid #61312 (Riabinina et al., 2015). To establish the driver line *Tg(ath5:QF2)*, a QF2-polyA; FRT-KAN-FRT;cmlc2:Cerulean fragment was PCR amplified and inserted into the ath5 BAC clone DKEY-111E19 using BAC recombineering as described previously (Förster et al., 2017). The resulting Tol2-ath5:QF2 BAC (100 ng/μl) was co-injected with transposase mRNA (50ng/μl) into TL/nacre zebrafish eggs. Cmlc2:Cerulean expressing larvae were raised and identified as founders by an outcross by an outcross to *Tg(QUAS:GFPcaax)* fish. Stable *ath5:QF2* transgenes could then be crossed to *Tg(QUAS:GCaMP6s)* or *Tg(QUAS:epNTR-TagRFP)* fish.

METHOD DETAILS

Visual competition behavioral assay

We designed a setup to project looming stimuli to 9 individual zebrafish larvae simultaneously via a screen below the animals. We adapted a previously described virtual reality setup which allows real-time tracking and presentation of arbitrary visual stimuli at animal-centric positions (Larsch and Baier, 2018). Animals were monitored individually in shallow glass dishes of 10 cm diameter separated by opaque walls to prevent visual contact. The dishes rested on a projection film for visual stimulation, confining the animals' distance to the screen to approximately between 3 mm and 13 mm by the rounded bottom of the dish and the surface of the water. To minimize stimulus distortion due to refraction at the air-glass-water interfaces, we submerged the projection film and glass dishes in water. Animals were recorded at 30 fps with cameras using the CMV4000 sCMOS chip (IDS UI-3370CP-NIR or PointGrey Grasshopper GS3-U3-41C6NIR-C) at a resolution of 2048x2048 pixels. We used a 25 mm lens (Edmund Optics Nr. 86-572) at a distance of 800 mm resulting in an image resolution of 150 um/pixel. Visual stimuli were projected onto the projection film from underneath via a cold mirror. Diffuse Infrared illumination for imaging was provided from below. Visible light stimuli (peaks around 450 nm, 525 nm and 625 nm) were provided to the fish via the projector (Optoma ML750ST, RGB values (255,255,255) for white) but blocked before the camera by an NIR band-pass filter.

Real-time processing of images and stimulus generation were performed on a Desktop PC running Bonsai (Lopes et al., 2015). Briefly, each camera frame was background subtracted and an empirically determined threshold was applied to isolate animals against the background. Next, contours were extracted to compute the center of mass and orientation of each animal. Based on animal positions and a stimulus property file, we generated animal-centric visual stimuli using custom Python scripts in Bonsai to control OpenGL drawing routines. Stimuli were dots (for black, RGB value (0,0,0)) on white background (RGB value (255,255,255)) unless noted otherwise. Dot size was a multiple of projected pixel size (1pixel was 0.47 mm side length). Looming stimuli were presented as stationary dots expanding for 500 ms (15 frames) with a linear increase in diameter. Stimuli were presented 1 cm from the

fish at angles of 45°, 90°, 135°, 180°, 225°, 270°, or 315° relative to the animals' center of mass and orientation at the beginning of the stimulus. Loom stimuli were presented once per minute. A moving grating was presented for 20 s ending 10 s before the presentation of the next loom stimulus to drive larvae toward the center of the dishes. At each frame, animal and stimulus parameters were streamed to a text file for offline analysis. The program also stored the video data after background subtraction into an xVid compressed .avi file via FFmpeg (ffmpeg.org) for later inspection. Camera and projector were aligned using a separate Bonsai routine before every experimental day as described previously (Larsch and Baier, 2018). Animals were tested at 5–8 dpf in fish water at room temperature (22–25°C). Before behavior testing, animals were kept in a Petri dish floating above a fully lit portion of the projection screen to allow habituation to light and temperature conditions of the experiment. Animals were analyzed for 60 to 300 minutes. The order of different stimuli was randomized for each group of 9 animals.

Data analysis for behavioral experiments with competing looming stimuli

Exported text files containing behavioral data and stimulus parameters were analyzed offline using custom-written Python scripts. We classified responses as escapes if the distance to the original position at the end of the expansion time of the stimuli (500 ms, after 15 frames) was at least 5 mm (approximately one fish body length). Distance from the initial position was defined as the Euclidean distance from the origin to a point in the x-y plane after 500 ms (end of stimuli expansion). The distance modulation of escape behaviors is in agreement with a previous study (Bhattacharyya et al., 2017) and was used as an indication of stimulus strength. Circular behavioral data statistics were performed with the python version of pycircstat (Berens, 2009); <https://github.com/circstat/pycircstat>).

Modeling

All models were implemented in Python, using NumPy and SciPy libraries. All models are based on repeated random sampling, where one stimulus response from an S1 trial and one stimulus response from an S2 trial are combined. The repetition of this sampling procedure generates a distribution of combined responses. The averaging model combines the pair of responses by taking the vector average of the response angle. In agreement with the reduced amount of backward responses, we implemented a mechanism to reduce the prevalence of such escapes in our model by redistributing backward swims to other headings. The winner-take-all model chooses randomly between the S1 response and the S2 response (effectively adding the S1 and S2 response distribution). The mixture model implements a random assortment between the winner-take-all model (with mix probability p) and the averaging model (with probability $p-1$). Distributions are plotted using a kernel density estimate (KDE) plot, with a von Mises (circularized) distribution. The mix model with bias was optimized using cross-validation and a grid search over parameter space. To compare the similarity of distributions, a circularized version of the energy distance metric was used. The plot in 1K and 1M quantifies the energy distance between models and real data, using many repeated generations of each model (which is stochastic, since the models themselves are based on random sampling from the real data). To generate a p value comparing model performance, we used a permutation test on the difference in energy distance to real data.

Prey capture experiments

Prey capture experiments were performed as described previously (Mearns et al., 2020). Briefly, we made a square chamber (15 × 15 mm, 5 mm deep) with walls made from 2% agarose. Individual larvae were introduced to the chamber with a drop of dense paramecia culture (*Paramecium multimicronucleatum*, Carolina Biological Supply Company, Burlington, NC). The setup was lit from below with an IR LED light source, and larvae were filmed for 20 minutes at 500 fps with a high-speed camera (Photofocus MV1-D1312-160-CL, Switzerland). The analysis was performed offline with custom-written Python code. We extracted the outline of the fish from each frame by finding the largest contour following background subtraction and thresholding. A second threshold was then set to extract contours of the eyes and swim bladder. We used the image moments of these contours to calculate the angle of each eye. Eye convergence in each frame was calculated as the difference between the eye angles, with positive values corresponding to eye convergence, zero corresponding to eyes parallel, and negative angles corresponding to eye divergence. For each animal, we defined the threshold for prey engagement as the local minimum of the bimodal distribution of eye convergence angles across all frames and defined the prey capture score as the proportion of time the fish spent engaged in prey capture.

Swim bouts were segmented automatically using a change point algorithm on the derivative of the tail angle with respect to time. J-turns were defined as any bout where the eyes were unaligned prior to the bout onset and converged by the end of the bout (i.e., the first bout in any hunting episode when the prey are first detected). Bout integrals were calculated by summing the tail angle values over the duration of a bout.

Calcium imaging

Zebrafish larvae were embedded in 2.5% low melting point agarose (Invitrogen). Visual stimuli were generated using custom Psychopy2/Psychopy3 scripts (Peirce et al., 2019) and consisted of black looming stimuli. For prey competition (Figures S4A–S4C) movies from recordings of real paramecia were binarized and scaled, keeping important parameters such as kinetics and size in agreement with previous work (Semmelhack et al., 2014). For quantification of the number of neurons before and after two-photon ablation of neurons the stimuli consisted of six presentations (three times in nasalward direction and three times in temporalward direction, alternating order) of a prey-like (8° dot, kinetics extracted from the same real paramecia movie described above, red on

black), followed by three presentations of a black looming stimulus (expanding 60 deg/s for 2 s) and three presentation of a dimming stimulus (red to black, 2 s).

The minimum distance between competing stimuli resulting in non-overlapping receptive fields was determined in pilot experiments to be at least 30 degrees in visual space. The centers of the two looming stimuli are 60 degrees apart, and at full expansion, the stimuli are 45 degrees, 30 degrees, or 15 degrees apart (for conditions where both stimuli are equal and expansion rate is, respectively, 30 deg/s, 60 deg/s, and 90 deg/s). Visual stimuli were projected onto a white diffusive screen using the red channel of a LED projector (LG, Model No. PA72G) from the side (animal distance to the screen was approximately 4cm) and a DLP® LightCrafter 4500 development module from the bottom (animal distance to the screen was approximately 1 cm). For full emission spectrum of projectors see:

https://github.com/amgfernandes/Imaging_analysis/tree/master/Projector_measurements.

Size of the stimuli (in degrees of visual angle) was adjusted taking into account the size of the projection and distance to the fish using Psychopy2/Psychopy3 Monitor Center. For monocular stimulation, we presented both from the side and bottom. Results were similar for both conditions. The 2P microscope used for imaging and holographic optogenetics is based on a modified Femtonics 3DRC (Femtonics, Hungary) driven by a Ti:Sapphire laser source (Chameleon Ultra II, Coherent) (see [Dal Maschio et al., 2017](#)). An electrically tunable lens placed just before the galvo scanner (ETL, Optotune, EL-10-30-Ci-IR-LD-MV) was used to enable fast remote refocusing. For [Figure S3A](#) we used a remote-Z-scanning module with a resonant 2P microscope. The module consists of a second objective and a piezo-modulated mirror, which allows us to shift between conjugated focal planes in the fish brain with high frequency.

Two-photon computer generated holographic (2P-CGH) optogenetics

For more details of the holographic approach see [Dal Maschio et al. \(2017\)](#). For experiments in the absence of visual stimuli, we stimulated Lhx9 NI cells with 920 nm excitation for 1000 ms, while recording the activity of tectal neurons with GCaMP6s at 1,020 nm (both cytosolic and nuclear version of GCaMP6s were used). Only cells that showed an increased activity of at least 15% when compared to baseline mean activity were considered for the analysis. This analysis also selects cells with strong spontaneous activity (this was very common for ChR2 negative control fish). For experiments with visual stimuli, optogenetic stimulation of ChR2 positive neurons was performed with 920 nm excitation with a total duration of 1000 ms (photostimulation started 500 ms before the visual stimulation and ended 500 ms later at the end of visual stimulation). Visual stimulation consisted of a single looming stimulus presented from the side (total duration of expansion of 500 ms, 60°/s expansion rate). Imaging was performed simultaneously with GCaMP6s at 1020 nm.

Genetic ablation of neurons

Larvae expressing *Tg(UAS:nfsb-mCherry)c264*, were treated with 7,5mM metronidazole (MTZ, Sigma Aldrich) in fish water containing 0.2% DMSO, typically for at a minimum of 8h. MTZ solution was washed three times and larvae were allowed to recover for at least 12h before imaging or behavioral experiments were performed.

Imaging analysis

Imaging analysis was performed with custom-written Python scripts. A regressor-based pixel-wise analysis of the imaging data was performed similarly to ([Miri et al., 2011](#)). Briefly, regressors are generated with time series that are set to zero for all time points except the time points of stimulation (visual stimuli), which are set to one. The regressors are then convolved with a kernel describing the GCaMP response function (GCaMP6s, tau-off = 1.8 s). *T*-scores for each pixel were calculated as in ([Miri et al., 2011](#)) and only pixels that passed an empirically determined threshold (using the 90th percentile) were used for further analysis. For [Figure 2I](#) a linear regression was used (Python `scipy.stats.linregress`). For ROI analysis, a linear regression approach was used (Python `scikit-learn`) similarly to [Helmbrecht et al. \(2018\)](#). We used the ordinary least-squares linear regression, $y = a + b_0x_0 + b_1x_1 + e$... (y representing the functional response, a representing the Y-intercept, b the coefficients (slope), x the regressors (independent variables) and e the random error term) to select ROIs. The coefficients of determination (R^2), were calculated using the `sklearn.linear_model.LinearRegression` method. R^2 was used to set a threshold removing ROIs with activity not locked to stimulus presentation (spontaneously active). The estimated coefficients for the linear regression problem were used to set a second threshold that selects ROIs fitting to the regressors used (time series set to zero for all time points except the time points of visual stimulation).

For quantification of holographic optogenetic activation effects, we generated a control distribution by shuffling the labels of trials with visual alone and trials with visual combined with optogenetic stimulation. This approach led to a normal distribution with a strong peak at around zero, used to set thresholds considered for quantification of enhanced and suppressed ROIs.

For quantification of the number of ROIs in both tecta before and after two-photon ablation of NI neurons, we used a method consisting of steps to identify functionally distinct cells, and then distinguishing prey-like, looming, and dimming-evoked responses. Extracted ROIs (see above) were clustered using hierarchical clustering (agglomerative approach with Python `scipy.cluster.hierarchy.linkage`) for visualization of response types. Regressors were created for each stimulus and convolved with a GCaMP6s kernel (see above) and a multiple linear regression (Python `sklearn.linear_model.LinearRegression`) was used to calculate R^2 scores of the regressors to the functional responses of each ROI. R^2 values were then used to set a threshold removing spontaneously active

ROIs. Afterward, the maximum score of either the prey-like stimuli (nasalward and temporalward), looming or dimming stimuli was used to assign ROIs to specific response types.

Optogenetic stimulation during presentation of looming stimuli

To perform optogenetic stimulation of the NI during the bilateral presentation of looming stimuli we used either *Tg(lhx9:Gal4VP16)mpn203*; *Tg(UAS:ChR2(H134R)-mCherry)mpn134* or *Tg(lhx9:Gal4VP16)mpn203*; *Tg(UAS:GtACR2-eYFP)sq212* double transgenic larvae. Controls were either sibling *lhx9:Gal4* larvae not expressing an optogenetic effector or *Tg(lhx9:Gal4VP16)mpn203*; *Tg(5xUAS:EGFP)zf82* larvae. In some experiments we used *Tg(lhx9:Gal4VP16)mpn203*; *Tg(UAS:ChR2(H134R)-mCherry)mpn134*; *Tg(UAS-E1b:Kaede)s1999t* larvae to photoconvert the stimulated region and confirm we were correctly targeting the NI.

We embedded 5-7 dpf larvae in 2% low-melting point agarose. After the agarose solidified, the dish was filled with Danieau's solution and agarose around the tail below the swim bladder was cut away using a scalpel, leaving the tail free to move and tested them the following day (6-8 dpf). Larvae were positioned between two LCD screens (LCD35VGAN, Accelelevision) displaying a white background. A 50 μ m light fiber (M24L05, Thorlabs), connected to a laser beam combiner (Lighthub, Omicron) to either stimulate (473 nm, LuxX 80 mW, Omicron) or photoconvert (405 nm, LuxX 60 mW, Omicron) neurons, was positioned over the NI via a microcontroller (MC1000e, Siskiyou). For stimulation, we used 0.5-2 mW power as measured at the fiber tip, pulsed at 30 Hz with a 50% duty cycle. We recorded tail movements at 350 fps with a Pike F032B camera (Allied Vision Technologies) positioned above the fish and backlit from below using a custom-built IR LED array.

We performed 6-14 trials per fish, with at least three minutes between trials. Every trial consisted of a 10 s pre-stimulation phase, followed by 3 s of light stimulation, and then a 10 s post-stimulation phase. In half of the trials for each animal, we presented looming stimuli to both eyes simultaneously during the stimulation phase. In these "looming trials" a stationary black dot (5° visual angle) appeared on each screen 0.5 s after the onset of the optogenetic stimulation. After one second, the dots expanded at a constant linear rate (20-40°/s) for one second and then disappeared. Stimuli were controlled using the PsychoPy2 python library (Peirce, 2007). In photoconversion experiments, we switched to the UV laser and stimulated for 5 minutes (0.5 mW, 30 Hz, 50% duty cycle) after all experimental trials had concluded.

Analysis of optogenetic experiments

We excluded any animal that did not respond at least once to the looming stimuli. We tracked the tail of the fish using computer vision algorithms written in Python 3 ([Helmbrecht et al., 2018](#)). The tail angle was defined as the angular deviation of the tail tip from the midline of the fish, with negative angles signifying deflections toward the stimulated side. Individual swim bouts were identified using a custom-written bout detection algorithm as described previously (Mearns et al., 2020) ($n = 916$ from 48 fish). We defined light-evoked bouts as any bout whose onset occurred while the laser light was on, and prior to the onset of the expansion of the dots for looming trials. Loom-evoked bouts were defined as any bout that occurred during the expansion phase of the visual stimulus. Fish also performed spontaneous bouts outside the stimulation phase of the experiment, which were included to generate the bout space but not subject to further analysis. To generate the bout space we first excluded any bout whose standard deviation was greater than 50° and maximum absolute tail angle greater than 120° ($n = 35$), as these represented struggling behaviors that likely occur as a result of the fish being embedded rather than in response to optogenetic or visual stimulation. We computed three features for each bout: the bout integral (sum of all tail angles over the duration of a bout), the maximum tail amplitude (signed maximum value of the absolute tail angle), and the tail beat frequency (bout peaks were identified using the `scipy.signal.find_peaks` Python function). To identify bout types, we applied hierarchical clustering over these three features and identified a maximum in the silhouette score at three clusters (sklearn Python library). Note that, to ensure consistent boundaries between bout types for ipsilateral and contralateral swims, we ignored the signs of the bout features. We assigned the labels C-start, burst swim and slow swim to the clusters following post hoc inspection of the bouts belonging to each cluster.

Statistical comparisons were always between the control group and either ChR2(+) or GtACR2(+) animals and were performed using the `scipy.stats` Python library. Probabilities of evoking swims under different stimulation conditions (light only or light + loom) were compared using Mann-Whitney U tests. The number of C-starts and burst swims elicited under different stimulation conditions were compared using Mann-Whitney U tests. Differences in the distributions of maximum tail amplitudes were compared using a Kolmogorov-Smirnov test.

Two-photon ablation of neurons

We targeted inhibitory (GABAergic-positive) and excitatory (*lhx9*-positive) NI neurons for ablation based on their position and fluorescence (GFP, Dendra or mCherry) using a two-photon microscope. A line scan spanning each cell was performed for a total of three times (800 nm, for 10 ms each round with 1 s delay in between). The power used was dependent on the dorsal-ventral position of the cells (250 mW was used for dorsal areas and 330mW was used for more ventral areas). To validate that this approach led to specific ablation of single cells with minimal off-target damage we recorded the same neurons before and after the ablation protocol. The appearance of red autofluorescence after ablation in the target neuron but not in the neighboring neurons verified that this protocol was highly specific (see [Figure 6A](#); compare pre-ablation and post-ablation). Sham ablations consisted of ablating cerebellum neurons labeled by the *Tg(lhx9:Gal4)mpn203* line. We targeted approximately 30-40 cells for each line used (same number of cells as for real ablation experiments). Control not ablated fish were embedded in the same dish together with ablated animals and follow the same protocol, except for the ablation part. For behavior experiments, after ablation fish were unmounted from agarose and allowed to recover for at least 12

hours before behavior testing. For imaging experiments, the same tectal plane was recorded before ablation and one hour after ablation.

Single-cell reconstructions

For some single neuron labeling, the transgenic fish line *Tg(brn3c:GAL4, UAS:gap43-GFP)s318t* (BGUG) was crossed to the *Tg(lhx9:Gal4)mpn203* line similar to (Helmbrecht et al., 2018). This approach could not be used with other lines (e.g., *Tg(gad1b:-Gal4VP16)mpn155*) possibly due to low expression level. To overcome this problem, we devised another method to achieve sparse labeling by co-injecting a plasmid with a heat shock promoter expressing Cre (*hsp70l:cre*) together with a *UAS:Brainbow* plasmid (*UAS:Brb1.0L*; Robles et al., 2013). These constructs were co-injected with Tol2 mRNA into *Tg(lhx9:Gal4)mpn203* or *Tg(gad1b:-Gal4VP16)mpn155*; *Tg(UAS:nfsb-mCherry)c264* embryos. By calibrating the heat shock duration (heat shock in a water bath at 37°C for 5–45 min), the EYFP fluorescence from the *UAS:Brainbow* construct could be used to label single cells. Constructs were pressure injected at a concentration of 25–50 ng/μL into 1–4 cell-stage embryos. Larvae were screened using a confocal microscope for single labeled projection neurons and positive larvae were used to record a high-resolution (1024 × 1024 pixels) confocal stack. Labeling of some individual GABAergic neurons was also achieved by crossing the *Tg(gad1b:Gal4VP16)mpn155* line to a UAS:HaloTag line that expresses in a highly variegated fashion. Due to the highly variegated expression of the UAS-HaloTag, single neurons in the Gad1b pattern could be imaged and reconstructed. This approach is part of the mapzebrain project (<https://fishatlas.neuro.mpg.de/>; Kunst et al., 2019).

Confocal imaging and anatomical reconstruction of neurons

Before acquiring confocal stacks, fish were anesthetized with 0.02% tricaine. For single-cell reconstructions and generation of the brain atlas imaging was performed as described previously (Helmbrecht et al., 2018). The collected neurons were then traced using the software neuTube (Build1.0z) and confirmed by at least two independent tracers. For live-imaging rainbow experiments, no reference channel was available. However, in the YFP-channel the signal was strong not only for the single neurons but also for the auto-fluorescence of the skin. We took advantage of this and registered the whole-brain YFP-stacks to a standard brain of the skin auto-fluorescence using the Computational Morphometry toolkit (CMTK; <https://www.nitrc.org/projects/cmtk/>;) with the following settings: -awr 01 -T30 -X52 -C8 -G120 -R3 -A' -accuracy 0.8' -W' -accuracy 0.8'. This standard brain was generated by registering the red and green channel of 150 fish expressing *Tg(elavl3:lyn-tagRFP)mpn404* to the standard brain as described in Helmbrecht et al. (2018). The registered green channel of these fish was then averaged to obtain a standard brain of the skin auto-fluorescence. In experiments using fixed animals, fish were stained against GFP for single neurons and synapsin as a whole brain marker and registered to the fixed synapsin standard brain as described in Kunst et al. (2019). The skin-registered neurons were then bridged to the synapsin standard brain using the *Tg(elavl3:lyn-tagRFP)mpn404* channel. All reconstructed neurons were visualized in their common coordinate system (synapsin) using mapzebrain (<https://fishatlas.neuro.mpg.de/neurons/>; Kunst et al., 2019; Figure 7) or the single-neurite tracer ImageJ plugin (Figures S10A–S10D). Standard brain *s1020t* used in Figure S10D is part of the mapzebrain project.

In situ hybridization and immunohistochemistry

Stainings were performed according to published protocols (Fernandes et al., 2012). For antibodies used see Key Resources Table. Riboprobes for *adcyp1a*, *nmos1* and *lhx9*, were generated from cDNA and subcloned into the TOPO vector (pCR2.1-TOPO, Invitrogen). Sense probes were used as a negative control for newly cloned probes. Riboprobes for *gad1b* and *trh* (Löhr et al., 2009) were a kind gift of Wolfgang Driever. For Figures S4K–S4M, DAPI (28718-90-3, Sigma) was used to label nuclear DNA of cells.

QUANTIFICATION AND STATISTICAL ANALYSIS

For statistical tests, we used the Python SciPy, Numpy, Matplotlib, Seaborn libraries and GraphPad Prism version 7 for Windows. For imaging experiments, we preferentially selected fish with strong expression. All error bars used are mentioned in figure legends.

Quantification of arbor length and number of arborizations of NI cells

To measure the total length and number of arborizations of NI cells projections in the tectum we used a mask for the tectum part of the mapzebrain (<https://fishatlas.neuro.mpg.de/neurons/>) project and extracted the axonal part occupied by the axon terminals. Values were averaged for each population (inhibitory and excitatory) and analyzed with Python. Plots were made using the Seaborn library. Pairwise multiple comparisons were performed with Kruskal-Wallis H-test from the SciPy library, followed by post hoc tests (Conover's test) with the scikit-posthocs library (<https://scikit-posthocs.readthedocs.io/en/latest/>; related to Figures S10F and S10G).